THESIS

DOSE PROFILE SURROUNDING A WASTE REPOSITORY

Submitted by

Jenelle Parson

Department of Environmental and Radiological Health Sciences

In partial fulfillment of the requirements

For the Degree of Master of Science

Colorado State University

Fort Collins, Colorado

Spring 2014

Master's Committee:

Advisor: Alexander Brandl

Thomas Johnson
Robert Woody

ABSTRACT

DOSE PROFILE SURROUNDING A WASTE REPOSITORY

The waste repository analyzed is an interim storage facility that houses low and intermediate level conditioned radioactive waste. In total, it contains 9996 200-L waste barrels. The barrels are arranged in a crate geometry to ensure easy access to each barrel. The repository walls are 0.2 m thick with extra shielding (0.7 m) present on the west, north, and east sides of the repository. Instead of extra shielding the south side of the repository has a 5.25 m gap from the crates to the wall, allowing for crane maneuverability. The dose rate profile was analyzed using Monte Carlo N-Particle Transport eXtended (MCNPX) for the south, west, and north sides. The east side was not explicitly analyzed, because of the symmetry between the west and east sides. The dose rate was analyzed using f5 detector tallies and fluence rate to dose rate conversion factors from ICRP 21. Here, contributions due to skyshine and other wall effects are analyzed in detail. For the west and north side (where shielding was present), it was found that as distance from the source increases the dose rate initially increases logarithmically to a maximum and subsequently falls off following an exponential function. The initial increase in dose rate is significant with a peak dose rate as much as 300% of the dose rate at the wall and remaining elevated until approximately 60 m from the waste repository. A similar dose rate increase is not observed for the southern side of the repository; instead, the dose rate falls off with a power function corresponding to a function between that for an infinite plane and a point source. The dose rate profile was analyzed with and without repository structures, and the initial increase is only present with the repository structure. This indicates that the initial rise is due to the presence

of walls and/or roof. The shape of the dose rate profile closely follows observed skyshine functions at accelerator facilities. Skyshine and wall effects have been analyzed extensively for medical accelerator facilities, but are generally not considered for a waste repository; the work suggests that skyshine and wall effects may be more significant than previously thought and should be considered in the design and construction of waste repositories.

ACKNOWLEDGEMENTS

Before coming to Colorado, I was apprehensive and scared, but excited for the adventure ahead of me. I could never have dreamed of the amazing relationships that I have developed with my peers, colleagues, and the random friends I have made on my journey. I was equally surprised by the enrichment of my relationships with my friendships and professional relationships from my home state of Oregon. Thank you everyone so much for enriching my life and giving me more and more to look forward to with each passing day.

Professional

First of all, I would like to thank my amazing advisor, Alex Brandl. I am appreciative for you accepting me as a Master's student and offering to continue as my PhD advisor (seriously, do you realize what you've gotten into?). I appreciate our long talks ranging from particle physics to your professional experiences to mini golf to the Krampus. You have provided me endless guidance and have made the process incredibly enjoyable. Thank you for your patience, support, and understanding my quirky sense of humor. I look forward to the next several years as your student.

Thank you also to my other great professors, Thomas Johnson and Georg Steinhauser. T.J., I appreciate your guidance and support in classes, selecting summer internships, and future employment. I also appreciate your encouragement in having me teach the radiation detection class (ERHS 531). You have made me feel like a valuable member of the department and pushed me to succeed. I do also enjoy our random and often unexpected chats about the perils of the streets of Chicago – they have given me a very interesting perspective that often clashes with my childish fascination with the bean and the beautiful cityscape. Georg, although you are new to

the department, I already can tell that you're a great fit with the very interesting personalities of Alex and T.J. I have very much enjoyed learning radiation chemistry from you and look forward to the time to come.

In the same light, I would like to thank all my classmates. You have been an endless source of helpful information for classes and entertainment. I love how tightknit our year is and I wouldn't change it for anything! Thank you also to Dave Dolan for your amazing Squirrel Drive and to Marilyn Magenis for the laughs about classes and becoming my close friend.

In the development of this project I would like to thank Nuclear Engineering Seibersdorf for providing this project. Thank you also to Norbert Zoeger and Roman Koppitsch for your support in developing the model through repository drawings and answering any questions I have. Also, thank you for looking through the endless abstracts and presentations that I have created throughout the course of the project.

As anyone knows MCNP is a powerful, but a very frustrating program. Thank you Rafe McBeth for running the MCNP files on the CSU cluster and assisting in debugging code. In addition, I want to thank Thomas McLean and Dave Seagraves at Los Alamos National Laboratory (LANL) for your help in developing a repeated source structure. Thank you also for your help with MCNP that has been completely unrelated to the project; I have immensely enjoyed learning about all the intricacies of MCNP and am convinced that I will never completely understand it.

I would also like to thank my employers: Bob Morris at M.H. Chew & Associates and Radiation Protection at Palo Verde Nuclear Power Plant. Bob, thank you for giving me the opportunity to do consulting work for you. I have enjoyed gaining another health physics perspective of the nuclear industry and valuable experience in working on a truly diverse and

unique project. I also appreciate our chats at the Health Physics meetings and attending your Cider Festival at your orchard. I hope that we continue to have great collaborations together. To the folks at Palo Verde, all of you are amazing. I enjoyed my experience so much at the power plant and am very fortunate to have gotten both the nuclear engineering and health physics sides of nuclear power. Keep up the good work in keeping doses ALARA!

This publication was supported by Grant Number T42OH009229-06 from CDC NIOSH Mountain and Plains Education and Research Center. Its contents are solely the responsibility of the authors and do not necessarily represent the official views of the CDC NIOSH and MAP ERC.

Personal

Thank you so much to my family: without your support none of this would be possible. While you have provided much financial support in me furthering my education, I equally appreciate the emotional and spiritual support that you have my given me. Especially my sister Amanda – you are amazing and a constant inspiration; thank you for constantly supporting my dreams and listening to me rant about things that you are clueless about.

A big thanks goes out to all my friends: you help keep me sane. While it would be impossible to acknowledge each one of you here, I'll give it a shot. Thank you to my longtime friend Jenna; here's to fourteen years of laughs, adventures, and inappropriate conversations with strangers, and fourteen more! My friend Ashley, you have always made me laugh and feel loved; I'm so glad that we have continued to be friends and I know that we will be friends forever! To my friends Amelia and Natasha: we make a deadly trifecta, and no one will quite understand the bond we share. My OSU health physics and nuclear engineering friends, I am so fortunate to have shared my time with you and see how your careers and lives have continued to develop. My

CSU physics friends, you are the craziest bunch of people I have hung out with; you guys are too smart and socially awkward for your own good, and I love it! To Satchmo, you're great, but kindly quit jumping on me in the middle of the night and petting my face; it's really getting weird. Also to my roommate, whose east coast nuances I will never quite understand but at least are entertaining; you're cool by me.

My CSU health physics friends, here's to two years of crazy nicknames, collecting random office decorations, drinking until our livers cried but our woes disappeared, and inside health physics jokes that are utterly unexplainable. Keep it classy and I better see your faces at the Health Physics Society Meetings, where we will forget how many years have passed and fall back into our old steps.

DEDICATION

To my father, you will forever be in my heart

TABLE OF CONTENTS

LIST OF TABLES

LIST OF FIGURES

LIST OF SYMBOLS

α_D	number albedo
A	source activity
A_1	constant in logarithmic fit function
A_2	constant in exponential fit function
A_3	constant in power fit function
A_4	constant in linear fit function
B	build up factor
B_1	constant in logarithmic fit function
B_2	constant in exponential fit function
B_3	constant in power fit function
B_4	constant in linear fit function
d	detector radius
dA	area associated with detector point
$d\Omega_{\mathrm{p}}$	shrinking solid angle subtended by the source/collision point
$\delta\Phi$	contribution of each source point on fluence
$\dot{D}$	dose rate
$\dot{D}_0$	original dose rate
$\dot{D}_s$	scattered dose rate
$\dot{D}_{us}$	unscattered dose rate
E	photon energy
E_0	original photon energy

θ	angle with respect to the normal vector
θ_0	original angle with respect to the normal vector
J_{in}	inward flow of photons
J_{out}	outward flow of photons
λ	mean free path
μ	linear attenuation coefficient
μ_{en}	energy absorption coefficient
$\frac{\mu_{en}}{\rho}$	mass energy absorption coefficient
$\hat{n}$	normal vector of area
N_0	original number of photons
N_{us}	number of unscattered photons
$p(\Omega_p)$	probability that the particle will be scattered into the detector
ρ	density
r	source or collision point
r_p	detector point
R	distance from source to detector
R^2	coefficient of determination
$\mathcal{R}$	line beam response equation
S	source strength
t	time
φ	angle
$\dot{\Phi}$	fluence rate
$\dot{\Phi}_{us}$	unscattered photon fluence rate

$\dot{\Phi}_0$	original photon fluence rate
x	distance from repository structure
$\vec{x}$	vector connecting source and detector point
x_s	shielding thickness
W	particle weight
ψ	dihedral angle
Ω	solid angle
Ω_{p}	solid angle subtended by the source/collision point

INTRODUCTION

The ubiquitous use of radioactive material in the medical, research, energy, and construction industries has led to the production of large volumes of radioactive waste. The variety of applications for radionuclides in each industry leads to a variety of radionuclides, activity levels, waste forms, and ultimately different methods for waste management. The goal of waste management is to store radioactive waste in a safe form until it has decayed sufficiently. The waste must be chemically and biologically stable, such that it does not breach the disposal or storage facility. Additionally, the waste and facility must be shielded enough to keep on-site worker doses below limits (20 mSv per year international or 50 mSv per year in the U.S.) and off-site public doses below limits (1 mSv per year). This thesis analyzes the dose rate profile surrounding an interim storage facility.

Radioactive Waste

Radioactive waste is generated during the production of medical isotopes for imaging and therapy, the nuclear fuel cycle, fabrication of consumer products, production and use of sources in industry, and decommissioning of nuclear sites [1] [2]. Due to the variety of applications, the radionuclides in waste will vary greatly. Typical radionuclides that are produced in various industries are listed in Table 1 [3] [2]. Radionuclides in radioactive waste can be naturally occurring or anthropogenic; for instance, radioactive nuclides in mining and milling are all naturally occurring but have been concentrated in the process, while medical radionuclides are generally manmade [1].

Table 1 Typical Radioactive Waste Created in Various Industries [3] [2] [4]

Diagnostic [3]	^{125}I, ^{57}Co, ^{58}Co, ^{14}C, ^{67}Ga, ^{111}In, ^{201}Tl, ^{123}I, ^{131}I, ^{99m}Tc, ^{51}Cr, ^{59}Fe, ^{81m}Kr, ^{133}Xe
Therapeutic [3]	^{131}I, ^{89}Sr, ^{32}P, ^{137}Cs, ^{60}Co, ^{198}Au, ^{192}Ir
Research [3]	^{3}H, ^{35}S, ^{32}P, ^{33}P, ^{14}C
Mining and Milling [2]	^{222}Rn, ^{218}Po, ^{214}Bi, ^{214}Po, U, ^{226}Ra, ^{230}Th, ^{210}Pb
Fuel Fabrication [2]	^{238}U, ^{234}Th, ^{234}Pa, ^{226}Ra, U, Pu, Th
Reactor Operation [2]	^{13}N, ^{41}Ar, ^{89}Kr, ^{87}Kr, ^{138}Xe, ^{135}Xe, ^{58}Co, ^{60}Co, ^{59}Fe, ^{51}Cr, ^{3}H
Industrial Radiography [4]	^{60}Co, ^{137}Cs, ^{192}Ir, ^{75}Se, ^{170}Tm, ^{169}Yt

The radionuclides listed in Table 1 vary greatly in half-life, decay type, and decay energy [3] [2]. The radionuclide that is focused on in this thesis is Cobalt-60. Cobalt-60 is produced in a variety of ways in multiple industries; that combined with its high energy gamma emissions and medium length half-life, makes Cobalt-60 an ideal radionuclide to study radioactive waste management storage dose rates. Not only is Cobalt-60 likely to be present in the waste repository, but is likely to contribute to a measurable dose rate. Specifically, Cobalt-60 is used in irradiators for sterilizing medical equipment, food, and blood; as a source for medical radiotherapy, industrial radiography, and research [2] [3]. Cobalt-60 is produced by neutron activation of Cobalt-59. Cobalt-59 has a fairly large radiative capture thermal cross section (37.18 b) [5]. The following is the neutron activation reaction for Cobalt-59.

$$^{59}_{27}\mathrm{Co} + ^{1}_{0}\mathrm{n} \rightarrow ^{60}_{27}\mathrm{Co} \qquad \mathbf{1}$$

Cobalt-60 can be produced for commercial use by irradiation of Cobalt-59 in nuclear reactors or using a neutron source; or it is produced gradually in nuclear reactor components through activation of Cobalt-59 in stainless steel where it presents a significant nuisance during reactor operation or decommissioning. Cobalt-60 has a half-life of 5.2714 year and decays via

beta emission, as depicted in the decay scheme in Figure 1 [6]. Subsequent to the beta emission (E_{max}, 318 keV), two gammas are emitted with energies of 1173 and 1332 keV.

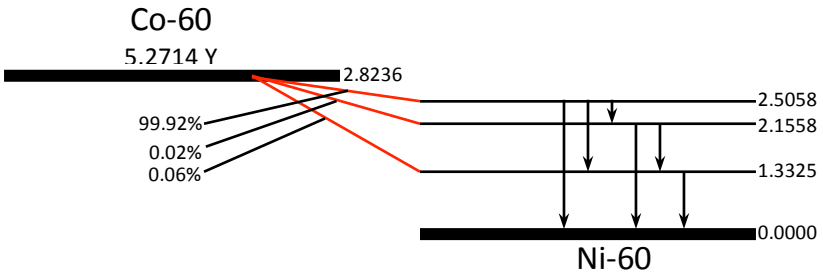

Figure 1 Cobalt-60 Decay Scheme [6]

Cobalt-60 is of interest in shielding and dose rate calculations due to the high energy of the two gammas emitted.

Radioactive Waste Classification

The International Atomic Energy Agency (IAEA) has identified six classes of waste: exempt waste, very short lived waste, very low level waste, low level waste, intermediate level waste, and high level waste [7]. IAEA classifications of waste are based on a safety assessment of individual cases, rather than an allowable activity based on radionuclide [7]. In the United States, there is no accepted standard classification scheme [8]. The U.S. Nuclear Regulatory Commission (NRC) has defined high-level radioactive waste and low-level radioactive waste (class A, class, B, and class C) [9]. The NRC defines waste based upon source radionuclide or total activity in the sample. Activities are limited based upon concentrations of long-lived radionuclides (Table 2) and the concentration of short-lived radionuclides (Table 3) [9]. If the sample contains multiple radionuclides, the activity concentration of each radionuclide is calculated and compared to values in Table 2 and Table 3 by taking the fraction. The fractions

are summed to calculate the effective radionuclide concentration to determine the waste classification. This method is otherwise known as the sum of the fractions rule.

Table 2 Concentrations of Long-Lived Radionuclides Used for Classification of Low Level Waste [9]

Radionuclide	Concentration (Ci/m^3)
^{14}C	9
^{14}C in activated metal	90
^{59}Ni in activated metal	220
^{94}Nb in activated metal	0.2
^{99}Tc	3
^{129}I	0.08
Alpha emitting transuranic ($t_{1/2} > 5$ yr)	100
^{241}Pu	3,500
^{242}Cm	20,000

Table 3 Concentrations of Short-Lived Radionuclides Used for Classification of Low Level Waste [9]

Radionuclide	Concentration (Ci/m^3)		
	Col. 1	Col. 2	Col. 3
Total of all nuclides ($t_{1/2} < 5$ yr)	700	Limited by external radiation and internal heat generation on transport, handling and disposal	
^{3}H	40		
^{60}Co	700		
^{63}Ni	3.5	70	700
^{63}Ni in activated metal	35	700	7000
^{90}Sr	0.04	150	7000
^{137}Cs	1	44	4600

Table 4 compares the IAEA classes of waste and the NRC category definitions [7] [9] [8]. The NRC defines waste based upon source or total activity in the sample, while the IAEA states that allowable activity is specified based upon a safety assessment of individual disposal sites [7] [9]. In this thesis, waste will be referred to according to IAEA classifications.

Table 4 Radioactive Waste Classification [7] [9] [8]

IAEA [7]		NRC [9]	
Exempt Waste	Is lower than clearance, exception or exclusion criteria		
Very Short Lived Waste	Will decay in a period of several years and discharged		
Very Low Level Waste	Does not require a high level of isolation and containment		
Low Level Waste	Is greater than clearance activity with limited long-lived radionuclides such that containment is only needed up to few hundreds of years	Class A	< 0.1 value in Table 2 < Col. 1 in Table 3
		Class B	0.1 – value in Table 2 Col. 1 – 2 in Table 3
		Class C	> value in Table 2 (generally not acceptable for near surface disposal) > Col. 2 in Table 3 if > Col.3 in Table 3, not acceptable for near surface disposal
Intermediate Level Waste	Requires disposal at depths of tens to hundreds of meters	Waste not defined as LLW or HLW [8]	
High Level Waste	Significant heat generation and requires disposal in deep, stable geological formations, several hundred meters or more in depth	1 Irradiated reactor fuel 2 Liquid waste from reprocessing facility 3 Solid waste converted from liquid waste [9]	

Waste Management

There are two main methods for waste management: storage and disposal [8]. Storage is the temporary placement of waste in a facility where the waste can be retrieved, whereas disposal is a permanent placement and the waste is irretrievable [8]. The waste management option chosen will depend on the type of waste [8] [7]. Additionally, storage and disposal waste management methods are not mutually exclusive; waste may be stored for a period of time before disposal to reduce heat load or until a facility is available.

Waste storage and disposal is based on a series of engineered, natural, and institutional barriers [8]. The first barrier is the waste form, whose physical and chemical properties prevent radionuclide mobility by solidifying the waste [9] [8]. In the United States, liquid waste must be

solidified or packaged in sufficiently absorbent material to prevent leaking [9]. The volume cannot consist of more than 1% liquid [9]. The waste also must be structurally stable and cannot be flammable or create toxic gases, vapors, or fumes [9].

The second barrier is the canister, which is generally a metal or ceramic canister [8]. The canisters used are often multiple purpose, such that the canisters can be stored temporarily on site, be transported to final disposal, and be fit for disposal [9] [10]. The canisters used undergo structural and materials evaluations [10].

The third barrier is the disposal medium and is a natural barrier that prevents or delays the waste from re-entering the biosphere [8]. In the case of geological repositories, the natural barrier would be the stable geological formation. The final barrier is due to human institutions, including monitoring and warning markers [8].

As previously mentioned, the waste management option chosen will depend on the classification of the waste. For very short lived waste, the preferred method is decay storage [7]. For very low level waste, landfill disposal can be used, because high levels of containment and isolation are not needed [7]. For low level waste, near surface disposal or shallow land burial methods are used [8] [7]. Intermediate level waste requires storage at a larger depth than near surface disposal (tens of meters to hundreds of meters) [7]. High level waste needs to be stored even deeper, using deep geological disposal [8] [7].

Prior to disposal, low, intermediate, and high level waste may be stored in an interim storage facility [8]. An example of a typical interim storage facility is the Central Organization for Radioactive Waste (COVRA) facility in the Netherlands. At this storage facility, both low level and high level radioactive waste are stored. Steel waste barrels are provided to individual sites producing waste, mostly medical facilities. After filling the drums, they are sent back to the

COVRA facility. At the COVRA facility, the drums are compacted and encased in concrete inside of a final disposal drum and placed in the low level waste portion of the interim storage facility. An image of a mock-up drum present at COVRA is displayed in Figure 2.

Figure 2 Low Level Waste Drum Mock-up at COVRA

Lids are not used on the drum tops, so that any changes to the concrete can be observed. The canisters are stored on their sides and labeled according to the level of waste, as specified by the government of the Netherlands. An image of the low level waste storage at COVRA is shown on the left side of Figure 3.

Figure 3 Low Level Waste Storage (L) and High Level Waste Storage (R) at COVRA

The high level waste at COVRA consists of processed reactor fuel and spent research reactor fuel. The fuel is stored in individual channels and is air cooled (see right side of Figure 3).

Dose rate profiles are developed for these facilities prior to construction to insure that shielding is sufficient to keep worker and public doses as low as reasonably achievable (ALARA). Many methods exist for modeling dose rate profiles surrounding radioactive sources, which will be discussed in the next section.

Developing Dose Rate Profiles

The dose rate at a detector location from a photon emitting radioactive source depends on the photon fluence rate and the photon energy (i.e., radionuclide), such that the dose rate can be expressed as:

$$\dot{D} = \dot{\Phi} E \frac{\mu_{en}}{\rho}, \quad \textbf{2}$$

where $\dot{\Phi}$ is the fluence rate, E is the photon energy, and $\frac{\mu_{en}}{\rho}$ is the mass energy absorption coefficient

The photon fluence rate at a given point depends on the solid angle subtended by the source onto the detector and scattering as the radiation moves through material between the source and detector. For point and small sources, this fluence rate follows the inverse-square law, such that:

$$\dot{\Phi} = \frac{A}{4\pi R^2}, \quad \textbf{3}$$

where A is the source activity and R is the distance from the source to detector

For area and volume sources, deriving smooth analytic functions for the fluence rate can be accomplished by integrating over all source points.

$$\dot{\Phi} = \int \frac{A(\vec{x})}{4\pi R(\vec{x})^2} d\vec{x}. \quad \textbf{4}$$

Depending on the complexity of the distribution of the source, integrating over each source point can be difficult. Some closed analytic functions for dose rates that have been developed include simple area and volume sources, such as line sources, planar sources on and off center, and on-center right circular cylinders [11]. In other instances, dose rate functions have been developed numerically and using Monte Carlo calculations.

Area and volume sources can be approximated as point sources. The distance at which this occurs, however, is not clearly defined. For line and disk sources, Bevelacqua calculated the

error at distances one, two, and three times the maximum dimension of the source [12]. Bevelacqua found errors for line and disk sources of 8% and 12% at one times the maximum dimension, respectively, 2% and 3% at twice the maximum dimensions, and 1% at three times the maximum dimension [12]. For area and volume sources, Johnson and Birky recommend a distance of greater than twice the largest dimension of the source [11].

While these estimates are sufficient for many small sources, in the case of large sources, such as a waste repository, where people work closer to the source than these few times the largest dimension of the volume source, dose estimation might not be sufficient. In a previous paper, the dose rate function for a standard six waste barrel arrangement was developed [13]. The dose rate function was divided into two regions for an arrangement of six waste barrels: a near region that followed a logarithmic decrease and a far region that followed a power function close to the inverse-square law [13].

Impact of Shielding Material

The equations for fluence rate (3 and 4) are simplifications and only include effects of source geometry on fluence rate. More accurately, when there is a material matrix associated with the source and its surroundings, there will be attenuation by that material. Attenuation is the gradual loss of intensity for a photon source due to scattering and absorption. The attenuation process can be described through an exponential function, and the number of unscattered photons (N_{us}) can be calculated through the following equation.

$$N_{us} = N_0 e^{-\mu x_s}, \quad \textbf{5}$$

where μ is the linear attenuation coefficient and x_s is the shielding thickness

The linear attenuation coefficient is the probability per unit distance traveled that a photon interacts in the material [14] [15]. The linear attenuation coefficient depends on the composition of the material and the energy of the photons. Often, the linear attenuation coefficient is normalized to the density of the material and is called the mass attenuation coefficient. The following figure displays a graph of the mass attenuation coefficient as a function of photon energy for various materials [15]. As seen in Figure 4, the mass attenuation coefficient is greatest for lower energy photons.

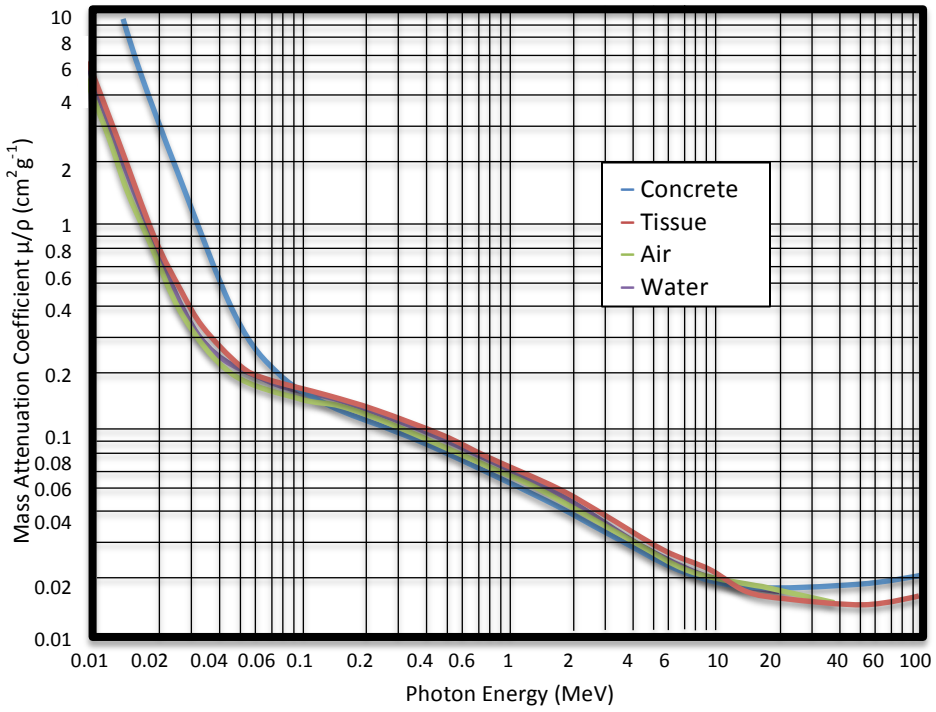

Figure 4 Mass Attenuation Coefficient (μ/ρ, cm^2/g) for Photons in Various Materials [16]

The unscattered photon fluence rate can then be described by:

$$\dot{\Phi}_{us} = \dot{\Phi}_0 e^{-\mu x_s}. \qquad \mathbf{6}$$

The photons that are scattered or absorbed by the shielding are not detected for a narrow photon beam and a thin shield ("good geometry", see Figure 5); such that the unscattered photon

fluence rate is equal to the actual photon fluence rate at the detector [15]. The shield must be thinner than the average distance between photon interactions (mean free path) to be considered a thin shield.

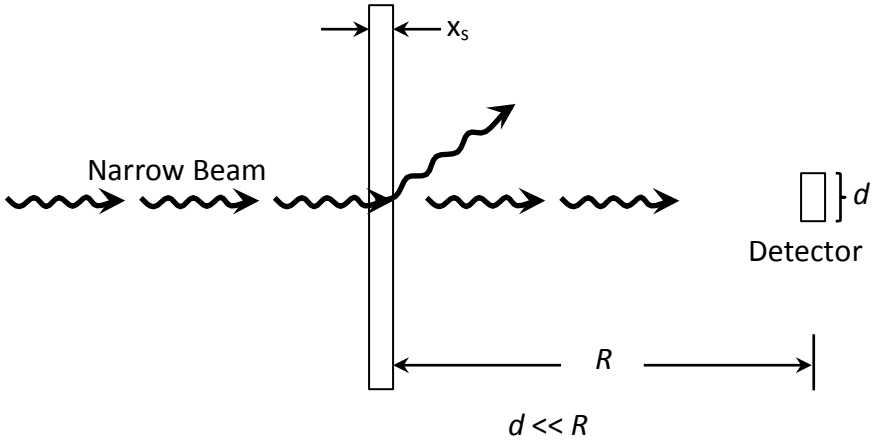

Figure 5 Photon Fluence Rate for Good Geometry at a Detector Location [15]

If the source geometry is not a "good geometry", the calculation of the fluence rate is complicated by buildup, photon albedo, and skyshine [14]. Buildup occurs in a shield as radiation is scattered back into the detector; therefore the unscattered photon fluence will underestimate the fluence at the detector location. A buildup factor (B) is used to account for build-up on the shield [14]:

$$B = \frac{\dot{D}}{\dot{D}_{us}} = 1 + \frac{\dot{D}_s}{\dot{D}_{us}}. \qquad 7$$

The buildup factor can have a large range of values depending on the thickness of material and the energy of the photons.

Figure 6 contains buildup factors for concrete for various energies and thicknesses (μx_s). Build up factors are greatest for larger thicknesses and lower photon energies for concrete [15].

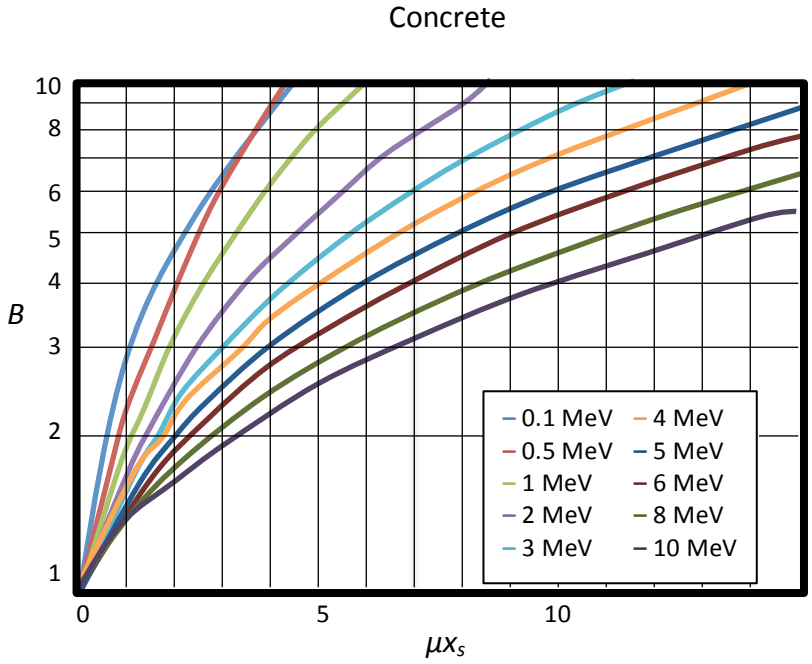

Figure 6 Buildup Factors for Concrete [15]

Similarly to buildup within a shield, photon albedo also causes an increase of fluence rate at a detector position due to scattering. Photon albedo is the reflection of photons in shielding or structural material [14]. The photons penetrate the surface of the material and emerge on the same surface at a different point in the material with a reduced energy [14] [17]. The result of photon reflection is a larger fluence rate at the detector position than the unscattered fluence rate. Photon albedo is described by the number albedo (α_D), defined as the ratio of the outward and inward flow of photons (J) [17]:

$$\alpha_D(E_0, \theta_0; \theta, \psi) = \frac{J_{out}(\theta,\psi)}{J_{in}}. \quad \mathbf{8}$$

The concept of skyshine is very similar to photon albedo, but involves the scattering of photons that are directed vertically [14]. The radiation is reflected to the ground at a distance far from the original source by the atmosphere. Skyshine can result in increased doses to workers or general public far from the source [14]. Figure 7 displays an illustration of skyshine for a vertically oriented source [18].

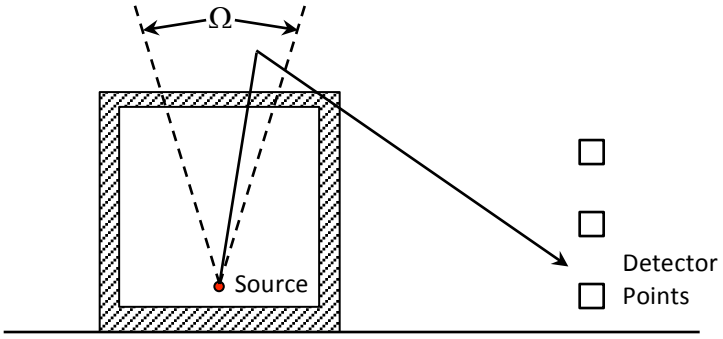

Figure 7 Illustration of Skyshine [18]

The calculation of skyshine is difficult and requires computationally intensive methods based on multidimensional transport theory [14]. Skyshine can be approximated using a line beam response function ($\mathcal{R}(E, \varphi, x)$), which gives the air kinetic energy released in matter (KERMA) for a distance R, angle φ, and photon energy E. The skyshine dose at a detector point can be calculated through the following equation [14]:

$$D(R)_{skyshine} = \int_0^{\infty} \int_{\Omega_s} S(E, \Omega)\, \mathcal{R}(E, \varphi, R) d\Omega dE, \qquad \mathbf{9}$$

where S is the source strength and Ω is the emission direction (solid angle)

Skyshine has been observed at accelerator facilities; notably facilities with insufficient roof shielding [19]. Accelerator skyshine has been further analyzed for the Varian Trilogy Linear

Accelerator at the Colorado State University Veterinary Medical Center by Elder [18] and for Varian 2100 C treatment rooms by McGinley [19]. Both works found an initial increase in photon dose rate, peaking around 300% of the original dose rate, and returning to original dose rate at around 30 m (Figure 8). Additionally, Elder found a similar, more pronounced increase when the gantry was not positioned vertically [18].

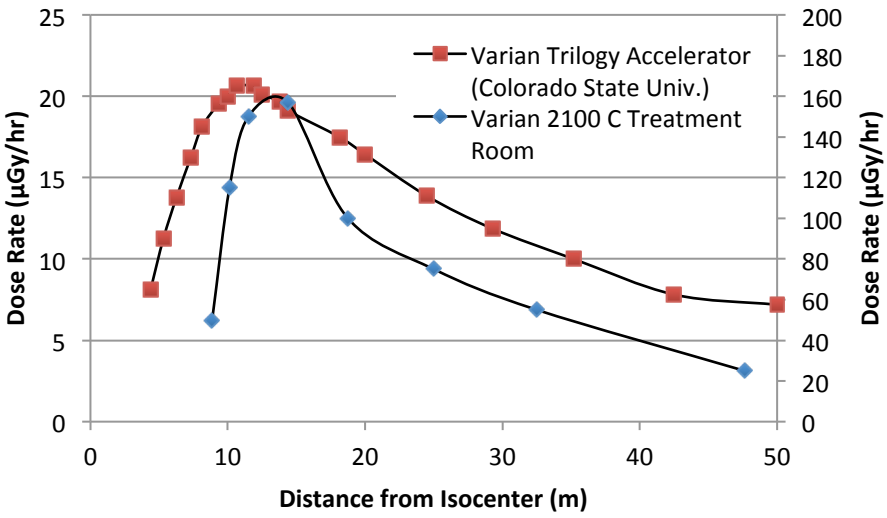

Figure 8 Skyshine Dose Rates for the Varian Trilogy Linear Accelerator at the Colorado State University Veterinary Medical Center (L) [18] and for Varian 2100 C Treatment Rooms (R) [19]

The dose rate can be described by the following equation where build up, albedo, and skyshine are taken into account

$$\dot{D} = B\alpha_D \dot{D}_0 e^{-\mu x_s} + \dot{D}_{skyshine}. \quad \textbf{10}$$

As previously mentioned, it can be difficult to develop closed analytic functions for complex geometries. Rather, numerical and Monte Carlo methods are often used. This thesis utilizes Monte Carlo methods, which will be discussed in detail.

Monte Carlo Codes

Two different types of codes are used to model dose rates: deterministic and Monte Carlo codes. Deterministic codes compute a mathematical function that does not vary based on iteration, such that the same input will always result in the same output. For instance in particle movement, the Boltzmann transport equation representing the average behavior of particles is solved [20]. Monte Carlo codes are computational algorithms that rely on repeated random sampling to obtain numerical results. In Monte Carlo programs that describe particle movement, individual particles are tracked and each interaction is derived based upon random sampling; the behavior of many particles (trials) is recorded and the average behavior is inferred [20]. Monte Carlo codes for radiation transport include the Monte Carlo N-Particle Transport (MCNP) code developed by Los Alamos National Laboratory, Electron Gamma Shower (EGS-NRC) developed by the National Research Council, and the FLUKA particle transport code developed by the Italian National Institute for Nuclear Physics and the European Organization for Nuclear Research.

The Monte Carlo code used in this thesis to derive dose rate functions is Monte Carlo N-Particle Transport eXtended, an extension of MCNP (MCNPX). MCNP follows each particle from source to death [20]. At each step of its life, probability distributions are randomly sampled using transport data to determine the outcome [20]. For photons, photon interaction tables are sampled which contain information on incoherent and coherent scatter, the possibility of fluorescent emission following photoelectric absorption, and absorption in electron-positron pair production [20]. Average quantities of the system are determined using tallies and running numerous particles.

In an MCNP input deck, there are three sets of cards. Each set of cards specifies information used by the code. The geometry is divided into cells corresponding to different regions of the geometry characterized by material and density. The cells are specified by the first set of cards. This set includes the bounds of the cells, cell density, and cell material. The second set of cards includes the surfaces used to create the cells in the first set of cards [20] [21]. The second set of cards are the surface cards. The surface cards are used to set bounds of cells and sources [20] [21]. The final set of cards contains the data cards, which specify the radiation source, materials, and tallies [20] [21]. Materials are specified by element and mass or atomic fraction. There are eleven available tallies in MCNPX, which describe different average behavior of particles. The following figure describes the input deck structure of an MCNP file [21].

Message Block {optional}
blank line delimiter {optional}
One Line Problem Title Card
Cell Cards [*Block 1*]
blank line delimiter
Surface Cards [*Block 2*]
blank line delimiter
Data Cards [*Block 3*]
blank line delimiter {optional}

Figure 9 MCNP Input Deck Structure [21]

The types of tallies available in MCNPX include a surface current (F1), average surface flux (F2), average flux in a cell (F4), flux at a point or ring detector (F5), energy deposition (F6), fission energy deposition in a cell (F7), and pulse height distribution in a cell (F8) [21] [20]. For the tallies preceded by a *, such a "*F", the tally is multiplied by the photon energy (except F6 and F7). Table 5 contains descriptions of the tallies in MCNPX.

Table 5 Description of Tallies in MCNP

Tally Type	Name	Description	Units	*F Units
Surface Current	F1	Each particle that crosses the specified surface, its weight is added to the tally	#	MeV
Averaged Surface Flux	F2	Estimated using a surface crossing estimator	#/cm^2	MeV/cm^2
Averaged Flux in a Cell	F4	The average flux is estimated by summing track lengths in the cell.	#/cm^2	MeV/cm^2
Flux at a Point or Ring Detector	F5	For each source particle and collision event, a deterministic estimate of the fluence contribution to the detector point is made	#/cm^2	MeV/cm^2
Energy Deposition	F6	Modified track length flux tally with reaction rate and energy-dependent heating function taken into account.	MeV/g	Jerks/g
Fission Energy Deposition in a Cell	F7	Modified track length flux tally with reaction rate and energy-dependent heating function (fission and gamma-ray) taken into account.	MeV/g	Jerks/g
Pulse Height Distribution in a Cell	F8	Provides the energy distribution of pulses created in a cell.	pulses	MeV

The tally used in this thesis is the F5 detector tally, flux at a point detector. The F5 detector tally is a next-event estimator that is a deterministic estimate of the flux at the point detector [20]. By using a next-event estimator procedure the particles do not actually have to make it to the tally to be counted. Therefore, the F5 detector tally is useful when it is unlikely for particles to reach the tally location [20].

The following situation is used to describe how the F5 detector tally operates. There exists a source or collision point at position "r" with a detector point at "r_p" that has an associated area "dA". The distance between the source and the detector can be described as "R". There exists a shrinking solid angle, dΩ_p, subtended by the source/collision point onto the shrinking detector area. [20]

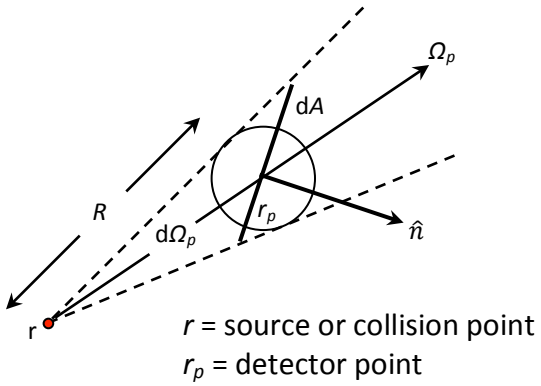

Figure 10 Description of F5 Point Detector Tally [20]

The contribution by the source/collision point *r* to the total fluence, $\delta\Phi$, can be calculated by determining the probability that the source particle will reach the detector [21] [20]. The probability of the source particle reaching the detector at r_p will depend on the probability that the particle will be scattered into the detector ($p(\Omega_p)$). Additionally, the probability of reaching the detector will depend on the probability of scattering along *R*, which can be described through the number of mean free paths between the source and the detector (λ). The contribution to the total fluence will also depend on the particle weight, *W*, such that the contribution for the source or collision point can be described through the following equation [21] [20]:

$$\delta\Phi = W \cdot \frac{p(\Omega_p)e^{-\lambda}}{R^2}. \quad \textbf{11}$$

The fluence can be calculated by integrating Equation 11 with respect to the solid angle, time, and photon energy. [20]

$$\Phi_p = \int\int\int \delta\Phi(\vec{r_p}, \hat{\Omega}, E, t) d\Omega dt dE. \quad \textbf{12}$$

The R^2 component in the denominator of Equation 11 causes the theoretical variance of the F5 detector tally to reach infinity [20]. As particles interact closer and closer to the detector, R approaches zero and the fluence approaches infinity [20]. An exclusion radius is specified around the detector point to exclude interactions that occur too close to the tally and cause errors [20] [21].

MATERIALS AND METHODS

Repository

The repository analyzed is an interim storage facility which houses low and intermediate level radioactive waste. The repository building extends 30.069 m in width, 61.332 m in length, and 8.31 m in height. The waste repository drawings used in creating the model were provided by Nuclear Engineering Seibersdorf. The following is a depiction of the waste repository using Visual Editor (VISED) [22].

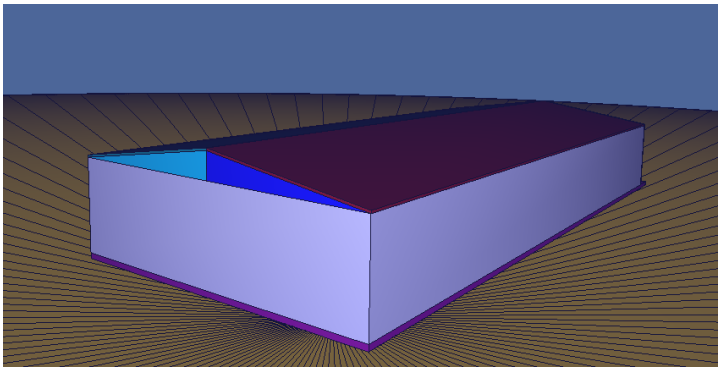

Figure 11 Model of Waste Repository Used for Analysis Rendered using VISED

Radioactive waste is first incinerated to reduce waste volume. The waste is then encased in concrete and poured into a 200-L steel waste barrel. A gap is left at the top of the waste barrel for expansion. In total, the repository houses 9996 waste barrels. The 200-L waste barrel dimensions are provided in Figure 12.

The drum has a total height of 88.6 cm with a radius of 28.15 cm. The walls of the barrel are 0.3 cm thick, while the bottom of the barrel is 0.5 cm thick. The air gap between the concrete and lid is 6.2 cm thick.

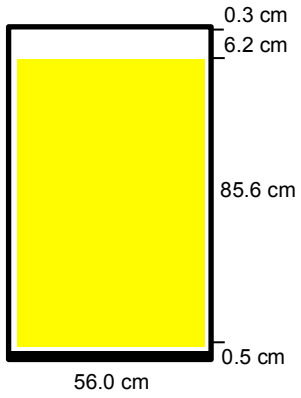

Figure 12 200-L Waste Barrel Used for Analysis

The four sides of the repository are denoted using cardinal directions in Figure 13, corresponding to the directions in bird's eye view (Figure 14).

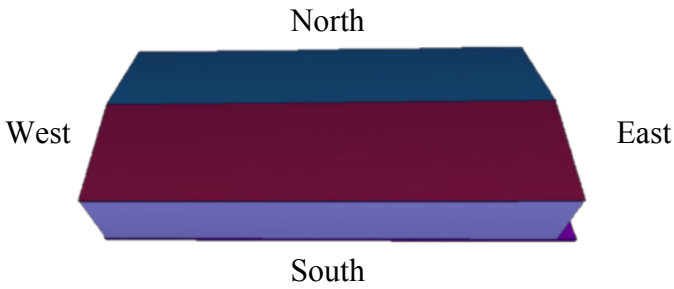

Figure 13 Nomenclature Used in Description of Waste Repository

The drums are stored back to back in a pallet of four drums for easy access to the tops of each waste drum. There are a total of 21 stacking rows containing 17 pallets. The rows are separated by 0.85 m to allow a person to walk between stacking rows. The pallets are stacked seven pallets high. Figure 14 shows a bird's eye view of the repository generated in VISED [22]. The 21 stacking rows appear vertically in Figure 14.

There is a distance of 1.0 m between the entire drum source and the walls of the repository for the west, north, and east sides. There is a 5.25 m gap between the drum source and walls for the southern side to allow for movement of a crane that moves waste drums. In addition to the 0.2 m thick wall on all sides, there is additional shielding on the west, north, and eastern

sides (0.7 m). The additional shielding is used to reduce doses outside of the repository, while the larger distance from the drum source to the wall is sufficient to reduce doses on the southern side.

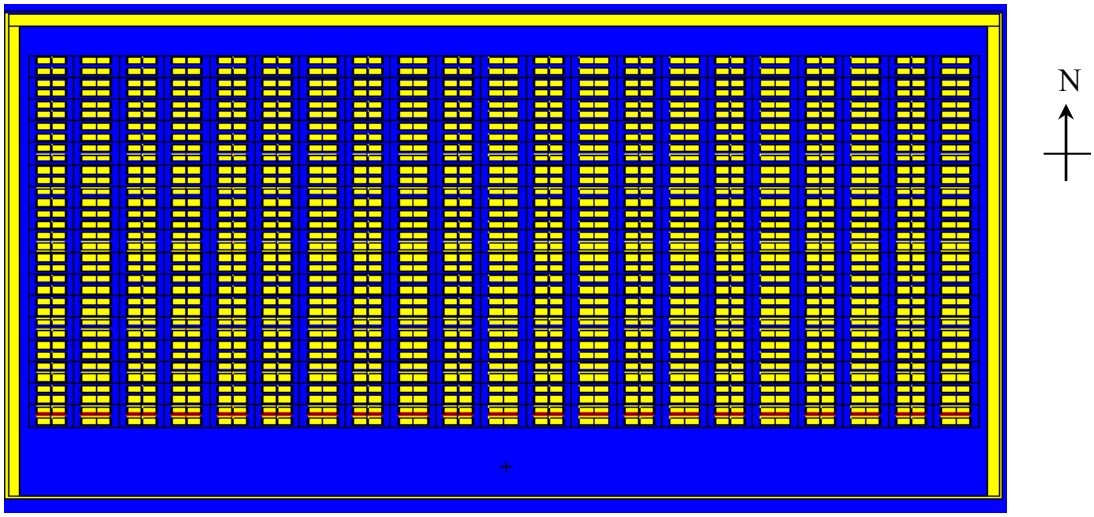

Figure 14 Bird's Eye View of the Repository

Figure 15 presents a view of the repository from the east side generated using VISED [22]. On the right side of Figure 15, the shielding on the northern side can be seen as well as the larger air gap on the southern side. The bottom of the drums in each stacking row can be seen.

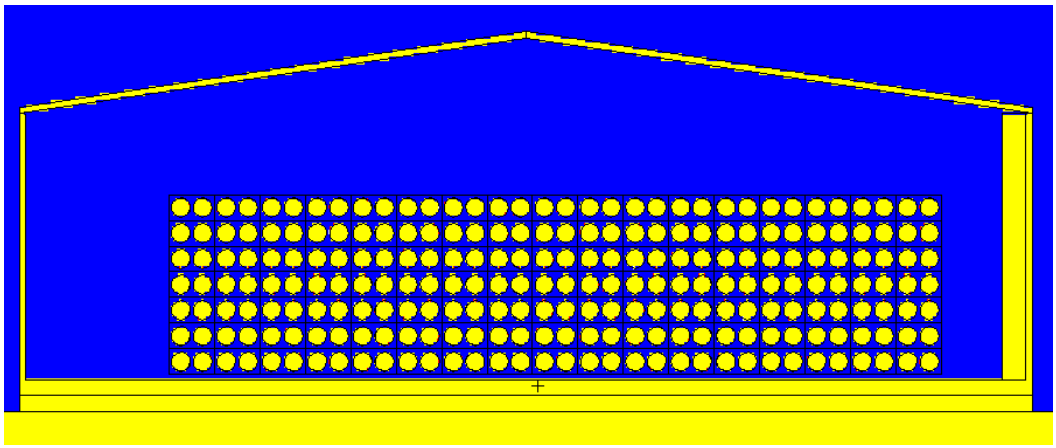

Figure 15 View from the East Side

Figure 16 is the view of the repository from the south side, also generated using VISED [22]. The shielding of the western and eastern side of the repository can be seen in Figure 16 as well as the 21 stacking rows.

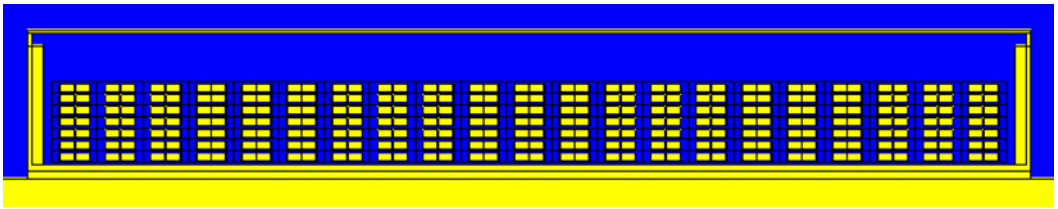

Figure 16 View from the South Side

Model

The entire drum source was modeled in MCNP using a repeated structure. The pallet of drums was specified and was repeated for the 21 stacking rows and seven stacked high. The drum contents were modeled as concrete according to material specifications in Table 6 with a density of 2.3 g/cm^3. The drum itself was modeled as pure iron with a density of 7.87 g/cm^3. Repository structures were modeled as pure concrete according to material specifications in Table 6 with a density of 2.2 g/cm^3. The dirt was modeled as concrete with a density of 1.2 g/cm^3, corresponding to the density of soil. The air was modeled as dry air near sea level with density and material composition in Table 6.

Table 6 MCNP Material Information

Material	Density (g/cm^3)	Atomic Composition	
		Element	Fraction[1]
Dry Air	1.124e-3	C_{nat}	*0.00125*
		N_{nat}	*0.755267*
		O_{nat}	*0.231781*
		Ar_{nat}	*0.012817*
Iron	7.87	Fe_{nat}	1.0
Concrete	2.3 (drum) 2.2 (structures)	^{1}H	0.1170
		^{16}O	0.6082
		N_{nat}	0.2748
Dirt	1.2	Same as concrete	

[1] Italicized denotes mass fraction, while non-italicized denotes atom fraction

The source was modeled as Cobalt-60 homogeneously distributed through the concrete contents of each drum. As seen by the Cobalt-60 decay scheme in Figure 1, two photons of energies 1.173 and 1.332 MeV are created in the beta decay. Cobalt-60 was chosen due to its high photon energy and will thus provide a worst case estimate of calculated dose rates. The source was modeled using a repeated cylindrical source structure. The transport of radiation through the geometry was simplified by only considering photon transport. In photon only transport, rather than producing electrons that deposit energy, the entire photon energy is deposited at the interaction point.

In determining dose rates, the F5 detector tally was used with an exclusion sphere radius of 1 cm. The fluence rate was converted to a dose rate using ICRP 21 fluence to dose rate conversion factors listed in Table 7.

Table 7 Fluence to Dose Rate Conversion Factors [23]

Fluence Rate (γ/cm^2-s)	Dose rate (rem/s)
<0.01	2.78E-06
0.01-0.015	1.11E-06
0.015-0.02	5.88E-07
0.02-0.03	2.56E-07
0.03-0.04	1.56E-07
0.04-0.05	1.20E-07
0.05-0.06	1.11E-07
0.06-0.08	1.20E-07
0.08-0.1	1.47E-07
0.1-0.15	2.38E-07
0.15-0.2	3.45E-07
0.2-0.3	5.56E-07
0.3-0.4	7.69E-07
0.4-0.5	9.09E-07
0.5-0.6	1.14E-06
0.6-0.8	1.47E-07
0.8-1.5	1.79E-06
1.5-2	2.44E-06
>2	3.03E-06

Detector tallies were used to develop dose rate profiles as a function of vertical height (vertical dose rate profiles) and dose rate function as a function of distance from the repository (horizontal dose rate profiles). Vertical tallies were taken at 20 m from the repository and encompassed the total height of the repository.

Horizontal dose rate profiles were developed for the west, north, and south sides of the repository for the following heights: 1.465, 2.605, 3.745, 4.4775, and 5.21 m. These heights correspond to the centerline of the first drum, halfway between the first and fourth drum, centerline of the fourth drum, halfway between the fourth and seventh drum, and centerline of the seventh drum (top drum). For the height of 3.745 m, the horizontal profile for the west, north, and south sides of the repository were also analyzed without walls.

HYPOTHESIS

This thesis analyzes trends in the vertical and horizontal dose rate profile of an extended radiological source arrangement. Expected dose rate profiles are discussed. The dose rate as a function of vertical distance is expected to increase until a maximum is reached at the center of the entire drum source. The first row of drums is expected to contribute the most to the dose, as reported by Brandl and Zoeger [13]; not only is the first row of drums located closest to the dose point, but the material within the drums will likely shield further rows (Equation 6). A maximum is expected, because the distance between the detector and the dose points in the first row of drums will be at a minimum, as seen in Equation 4. The dose rate is expected to continue to decrease with height after the dose tally height is greater than the height of the drum source, due to the larger distance between the top of the drum source and the tally point.

For the horizontal dose rate profile, skyshine is not expected to significantly contribute to the dose rate, in this study, due to the thickness of the roof [24]. Therefore, at close distances to the repository the drum source is expected to appear like an infinite plane source, such that the dose rate profile will follow:

$$\dot{D}(x) = \frac{\dot{D}_0}{x}, \qquad \textbf{13}$$

where x is the distance from the repository

At further distances from the repository, the dose rates from the repository are expected to behave less like an infinite plane source and begin to behave more like a point source. At a sufficient distance, the dose rate will correlate with the following equation:

$$\dot{D}(x) = \frac{\dot{D}_0}{x^2}. \quad \textbf{14}$$

At intermediate distances, the dose rate will neither follow the functional dependences for a line source or point source and will have an intermediate exponent value between 1 and 2 as a function of distance.

If the thickness of the roof of the repository is not sufficient and skyshine is present, dose rate profiles are expected to produce dose rate profiles similar to those derived by Elder [18] and McGinley [19] (Figure 8). The dose rate would initially increase with horizontal distance until a maximum is reached, and then decrease.

Vertical Profiles

Vertical profiles were developed for the north and west walls of the waste repository. The dose rate is displayed on the abscissa and the distance from the ground is displayed on the ordinate of Figure 17. Important geometry features are included in Figure 17, including the roof, drum source, and floor.

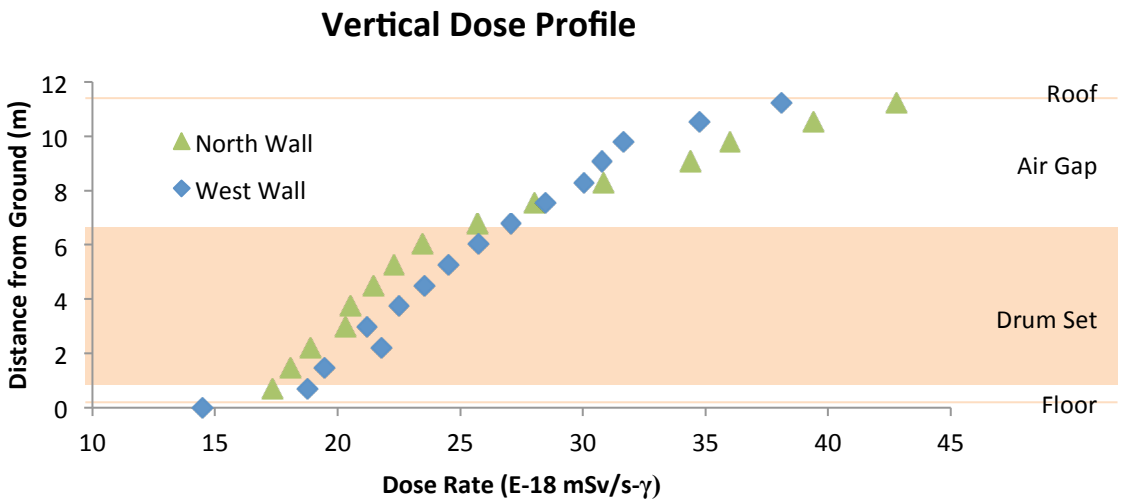

Figure 17 Vertical Dose Rate Profile for the North and West Walls of the Repository

Horizontal Profiles

The horizontal dose rate profiles were fit with smooth analytic functions within each dose rate region. Several regions were identified by visual inspection and by optimizing R^2 values for the trendlines. For the west and north walls, four different regions were identified: skyshine and wall effects regions characterized by a logarithmic increase and exponential decrease, respectively, an infinite plane region, and a point source region. The regions are illustrated in Figure 18.

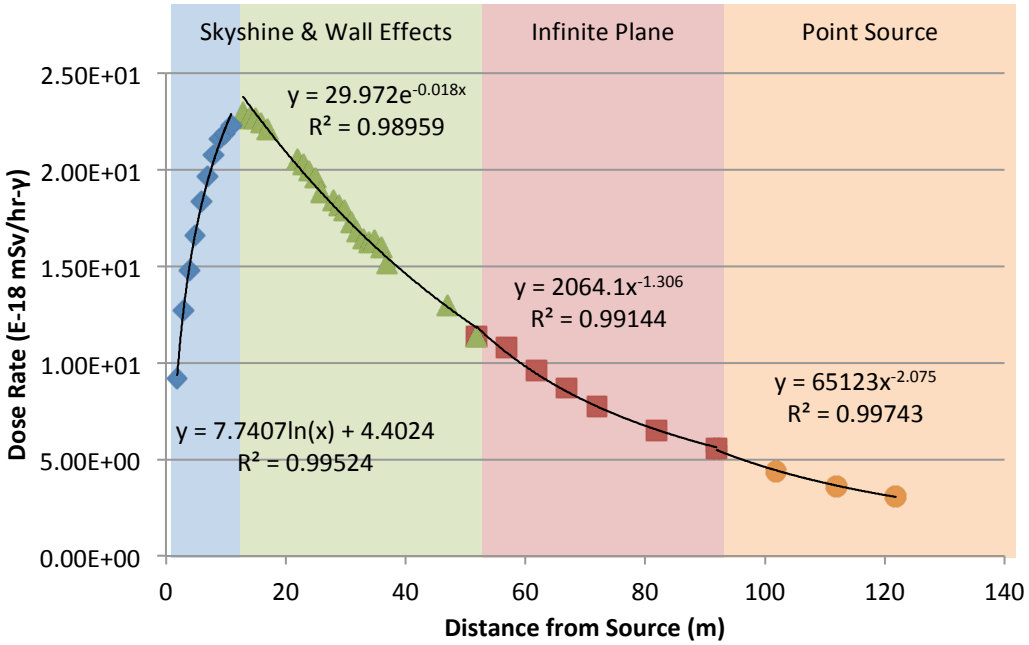

Figure 18 Typical Dose Rate Profile for the West and North Walls

The dose rate profile for the south wall was characterized by two regions: an infinite plane and a point source region.

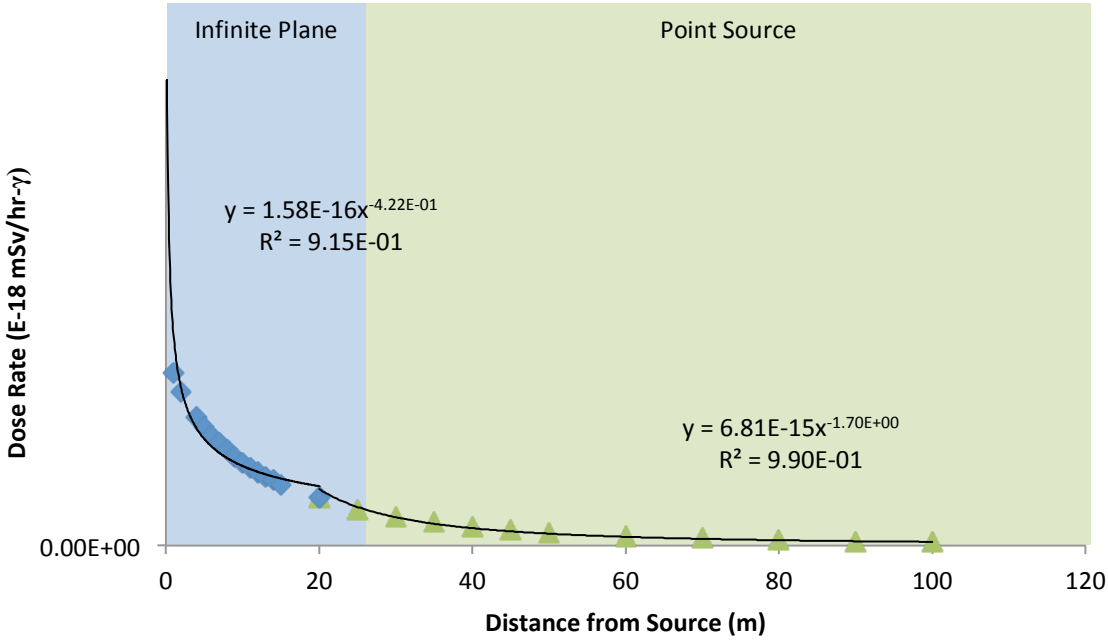

Figure 19 Typical Dose Rate Profile for the South Wall

The dose rate profiles for the north, west, and south walls were also analyzed without repository structures (walls and roof). The dose rate profiles follow the shape displayed in Figure 19.

The logarithmic portion of the wall effects and skyshine region is characterized by the following trendline, where A_1 and B_1 are constants:

$$y = A_1 ln(x) + B_1. \quad \textbf{15}$$

The exponential portion of the wall effects and skyshine region is characterized by the following equation, where A_2 and B_2 are constants:

$$y = A_2 e^{-B_2 x}. \quad \textbf{16}$$

The infinite plane and point source regions are characterized by a power function, where A_3 and B_3 are constants:

$$y = A_3 x^{-B_3}. \quad \textbf{17}$$

North Wall

The dose rate profile for all heights was divided into four regions as shown in Figure 18. Smooth analytic functions were fit to the regions corresponding to Equations 15 through 17. Fitting function information, including bounds of fitted regions and the R^2 value for the trendline, is presented in Table 8 and Table 9. Graphs used to derive the trendlines are presented in Appendix B. It should be noted that for the height of 5.21 m, dose rates were only evaluated to 36.9 m from the front barrel row. The following is a table containing the fit information for the skyshine and wall effects region for the north wall.

Table 8 Fit Information for the Skyshine & Wall Effects Region for the North Wall

Height (m)	Skyshine & Wall Effects							
	Logarithmic				Exponential			
	Region (m)	A_1 (E-18 mSv/s-γ)	B_1	R^2	Region (m)	A_2 (E-18 mSv/s-γ)	B_2 (m^{-1})	R^2
1.465	0-11.9	6.274	3.594	0.996	16.9-61.9	26.997	0.018	0.991
2.605	0-10.9	7.200	3.454	0.997	16.9-61.9	29.427	0.019	0.992
3.745	0-10.9	7.741	4.402	0.995	12.9-51.9	29.972	0.018	0.990
4.4775	0-8.9	9.962	3.607	0.992	12.9-61.9	32.819	0.020	0.998
5.21	0-7.9	12.743	2.244	0.992	12.9-36.9[2]	36.053	0.020	0.991

Table 9 contains information on the fitting function for the infinite plane and point source regions for the north wall. For most heights, only one region could be discerned. Therefore, the derived function does not correspond perfectly to an infinite plane or point source. Rather the function has a power value in between 1 and 2, corresponding to a transition region between a plane and a point source.

Table 9 Fit Information for the Infinite Plane & Point Source Regions for the North Wall

Height (m)	Infinite Plane				Point Source			
	Region (m)	A_3 (E-18 mSv/s-γ)	B_3	R^2	Region (m)	A_3 (E-18 mSv/s-γ)	B_3	R^2
1.465	61.9-101.9	4195.6	1.486	0.983				
2.605	61.9-101.9	3592	1.444	0.997				
3.745	51.9-91.9	2064.1	1.306	0.991	91.9-121.9	65123	2.075	0.997
4.4775	61.59-101.9	5045.5	1.51	0.987				

The infinite plane and point source regions identified exhibit similar B_2 and B_3 values to the expected power values to 1 and 2 as described in Equations 13 and 14, respectively. To ascertain how closely the regions follow these hypothetical functions for the height of 3.745 m, the infinite plane and the point source regions were force fit to Equations 13 and 14, respectively. Only the height of 3.745 m was chosen, because for this height the infinite plane and point

[2] For the 5.21 m height, tallies were only taken up to 36.9 m from the front waste barrel row

source regions could be identified individually. Equation 18 was derived for the infinite plane source region by optimizing D_0 based on the R^2 value.

$$y = \frac{580}{x} \qquad \textbf{18}$$

The derived trendline (Equation 18) is plotted with fitted data in Figure 20. To determine the degree of fit for the trendline, the coefficient of determination (R^2) was calculated as 0.948.

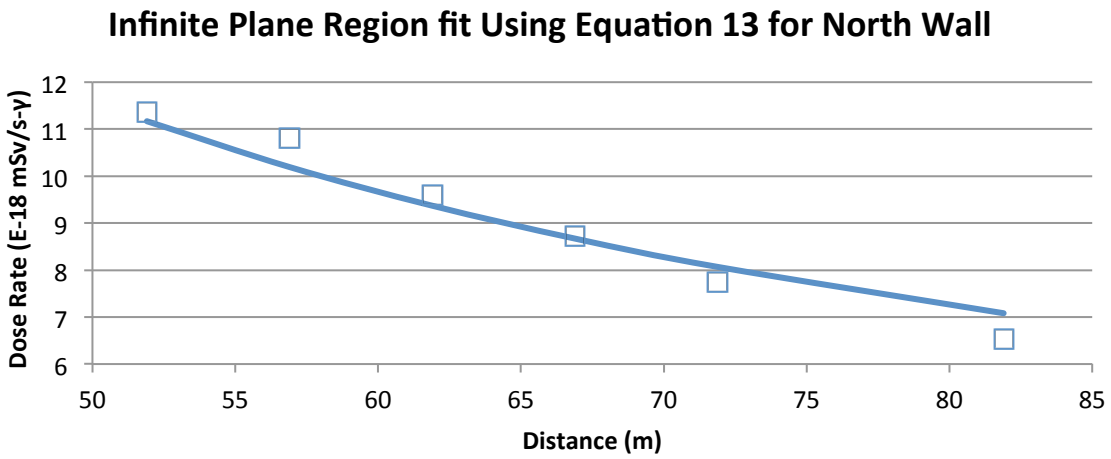

Figure 20 Infinite Plane Region Force Fit to Equation 13 for North Wall

Similarly, the equation for the point source region was derived by optimizing D_0 based on the R^2 value, and is shown in Equation 19.

$$y = \frac{465000}{x^2} \qquad \textbf{19}$$

The derived trendline (Equation 19) is plotted with fitted data in Figure 21. To determine the degree of fit for the trendline, R^2 was calculated as 0.994.

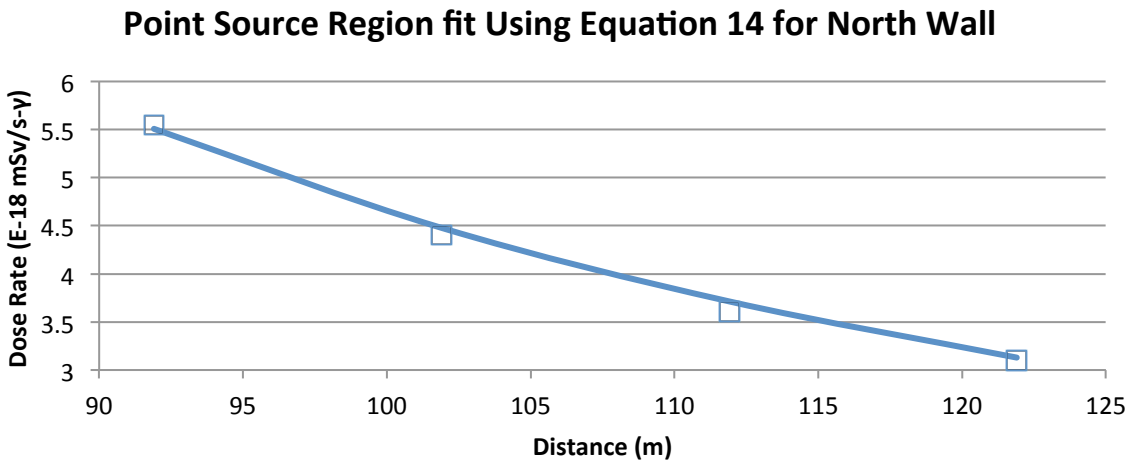

Figure 21 Point Source Region Force Fit to Equation 14 for North Wall

A plot of the dose rate profiles for the five heights is presented in Figure 22.

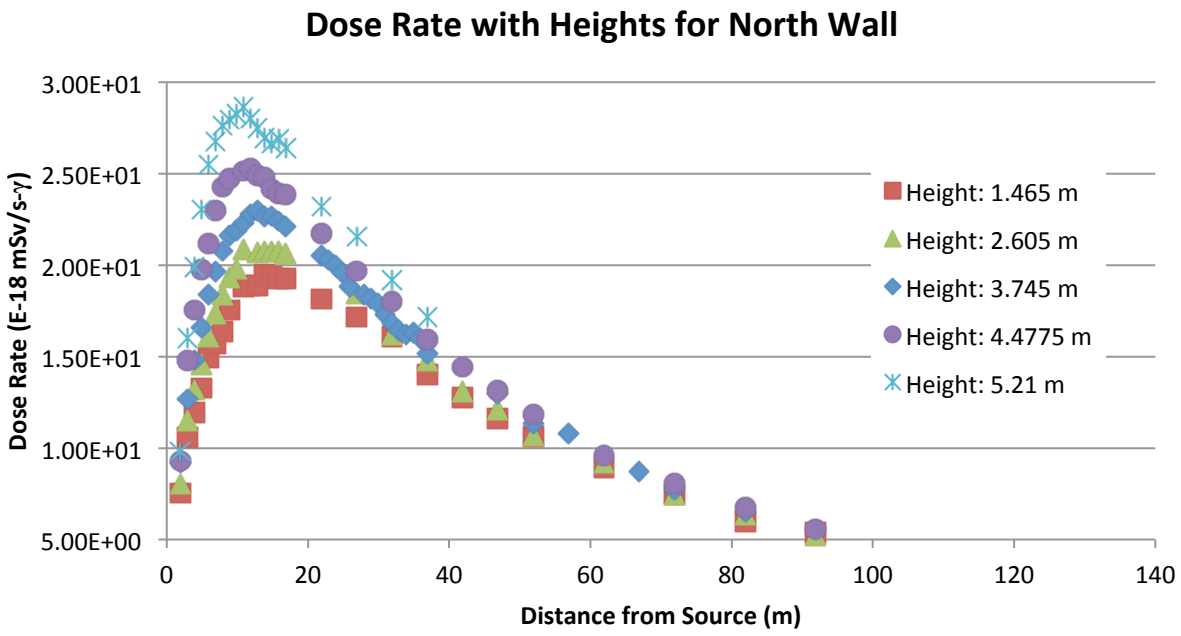

Figure 22 Dose Rate v. Distance for all Heights for North Wall

The location of the peak for each height was plotted against the vertical height of the tally (Figure 23). A linear function was fit to the data points, where A_4 and B_4 are constants.

$$y = A_4 x + B_4 \quad (20)$$

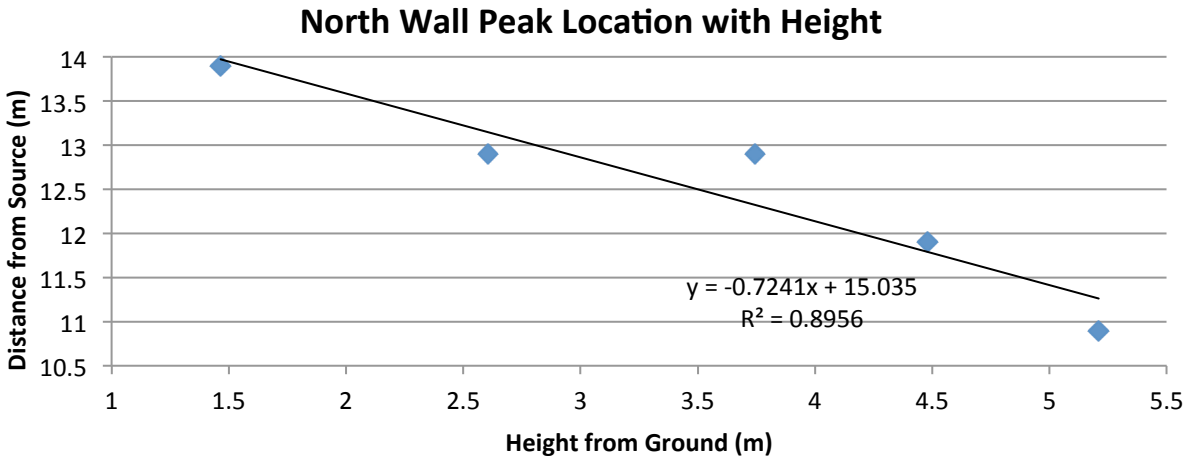

Figure 23 Peak Location v. Vertical Tally Height for North Wall

The dose rate profile for the north wall was analyzed with and without the repository structure at a height of 3.745 m. The following is a graph of the dose rate with smooth analytic fit functions for each region.

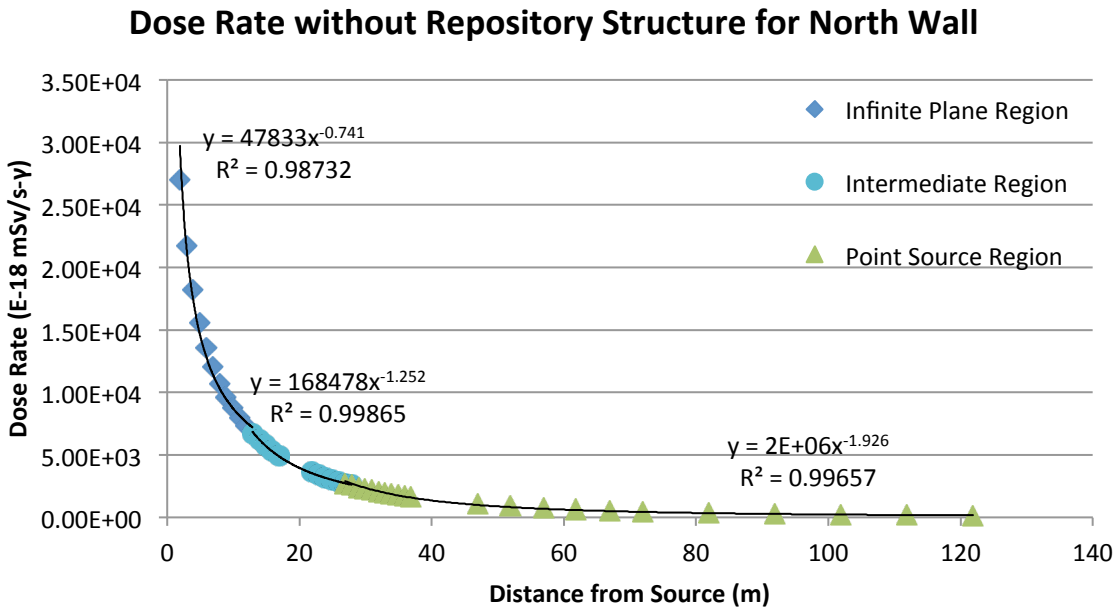

Figure 24 Dose Rate Profile Without Repository Structures for the North Wall

Figure 25 compares the dose rate profile with and without the repository structure. A logarithmic scale is used on the abscissa.

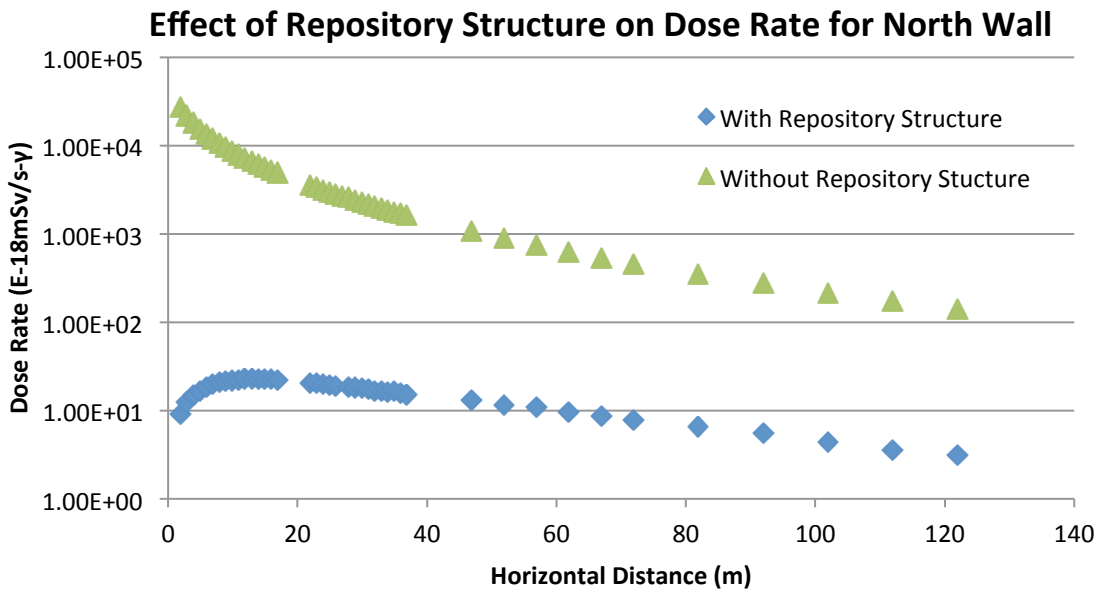

Figure 25 Dose Rate Profile With and Without Repository Structures for the North Wall

To ascertain the contribution that was not due to attenuation, the simulation without the repository structure was corrected for attenuation (Figure 26). When the curve without the repository is corrected for attenuation, the plot with the repository rises above the curve without the repository structure.

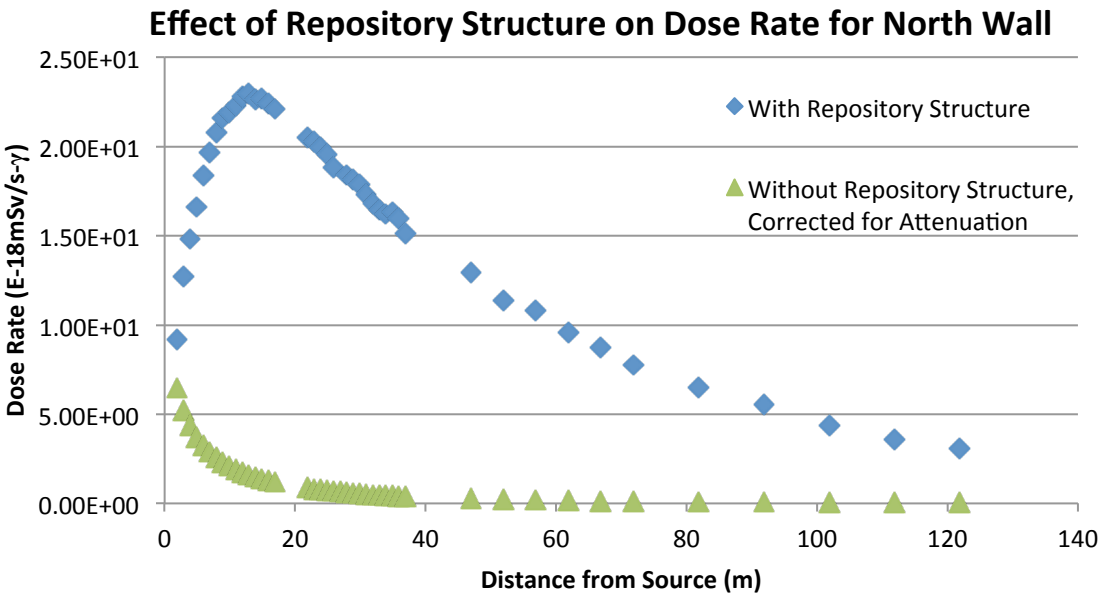

Figure 26 Dose Rate Profile With and Without Repository Structures (Attenuation Corrected) for the North Wall

The contribution due to effects besides attenuation was derived by subtracting the attenuation corrected dose rate without the repository structure from the dose rate with the repository structure.

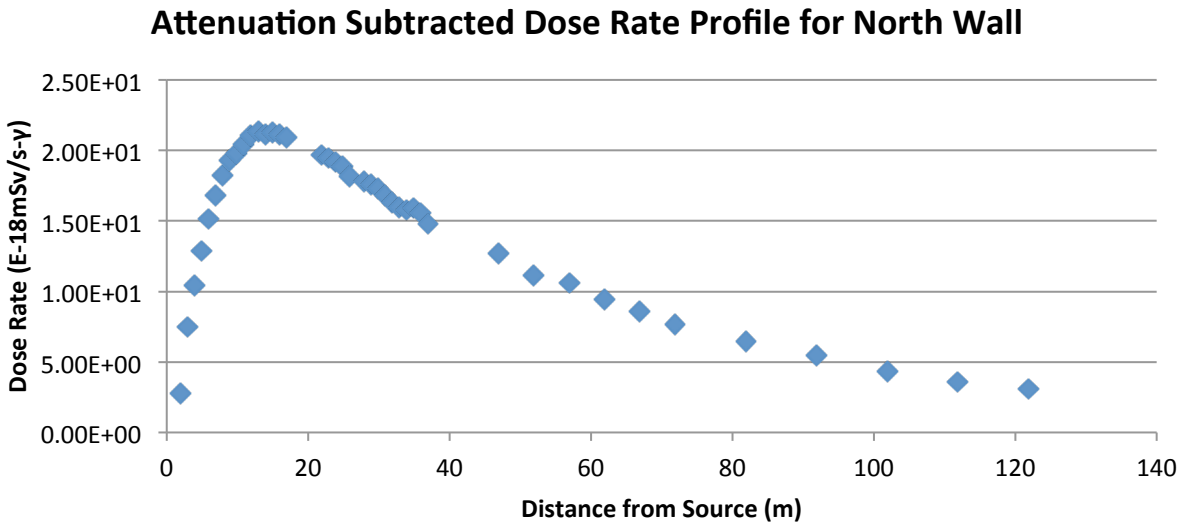

Figure 27 Non-Attenuation Contribution to Dose Rate Profile for North Side

West Wall

The dose rate profile for all heights was divided into four regions as shown in Figure 18. Smooth analytic functions were fit to the regions corresponding to Equations 15 through 17. Fitting function information, including bounds of fitted regions and the R^2 value for the trendline, is presented in Table 10 and Table 11. Graphs used to derive the trendlines are presented in Appendix B. It should be noted that for the height of 5.21 m, dose rates were not evaluated between 36.9 and 71.9 m. The following is a table containing the fit information for the skyshine and wall effects regions for the west wall.

Table 10 Fit Information for the Skyshine & Wall Effects Region for the West Wall

Height (m)	Skyshine & Wall Effects							
	Logarithmic				Exponential			
	Bounds (m)	A_1 (E-18 mSv/s-γ)	B_1	R^2	Bounds (m)	A_2 (E-18 mSv/s-γ)	B_2 (m^{-1})	R^2
1.465	0-11.9	9.828	-1.700	0.985	15.9-61.9	34.516	0.023	0.998
2.605	0-12.9	11.795	-2.395	0.988	13.9-61.9	37.863	0.024	0.995
3.745	0-10.9	14.465	-2.696	0.990	12.9-51.9	43.869	0.027	0.998
4.4775	0-8.9	20.867	-6.636	0.993	8.9-51.9	52.909	0.030	0.996
5.21	0-6.9	33.830	-15.103	0.994	9.9-36.9[3]	70.396	0.039	0.997

Table 11 contains information on the fit information for the infinite plane and point source regions for the west wall. For most heights, only one region could be discerned. Therefore, the derived function does not correspond perfectly to an infinite plane or point source.

Table 11 Fit Information for the Infinite Plane & Point Source Regions for the West Wall

Height (m)	Infinite Plane & Point Source			
	Bounds (m)	A_3 (E-18 mSv/s-γ)	B_3	R^2
1.465	61.9-101.9	5130.5	1.560	0.999
2.605	61.9-101.9	6672.9	1.607	0.996
3.745	51.9-101.9	3821.9	1.478	0.999
4.4775	51.9-101.9	5008.3	1.536	0.998
5.21	71.9-101.9	17545	1.807	0.989

A plot of the dose rate profiles for the five heights is presented in Figure 28.

[3] Data missing from 36.9 to 71.9 m

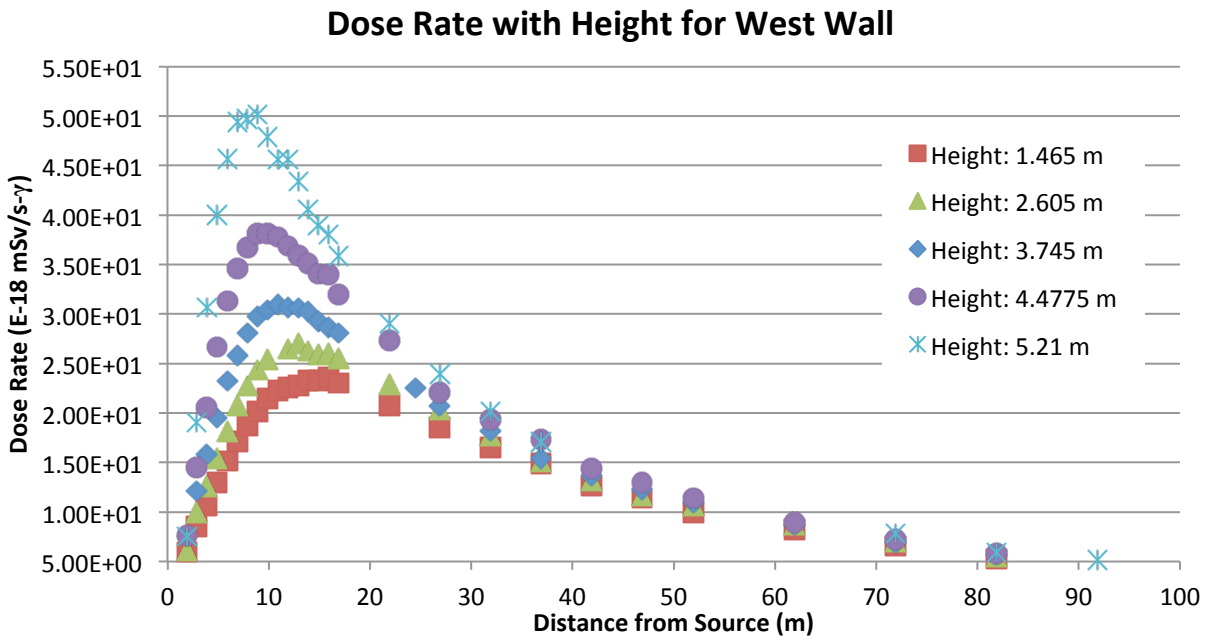

Figure 28 Dose Rate v. Distance for all Heights for the West Wall

The location of the peak for each height was plotted against the vertical height of the tally and a linear function was fitted to the data points based on Equation 20 (Figure 29).

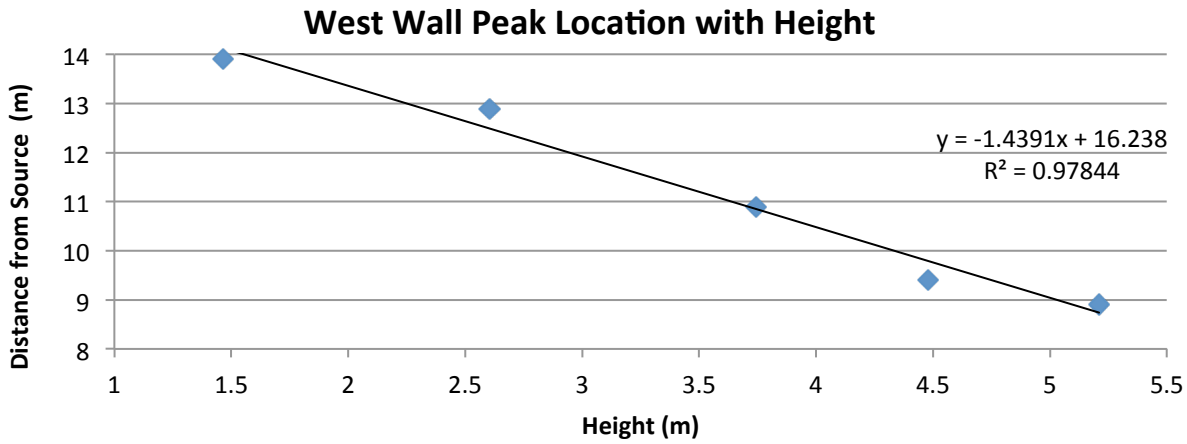

Figure 29 Peak Location v. Vertical Height for the West Wall

The dose rate profile for the west wall was analyzed with and without the repository structure at a height of 3.745 m. The dose rate without the repository structure was corrected for attenuation. The following is a graph of the dose rate with smooth analytic fit functions.

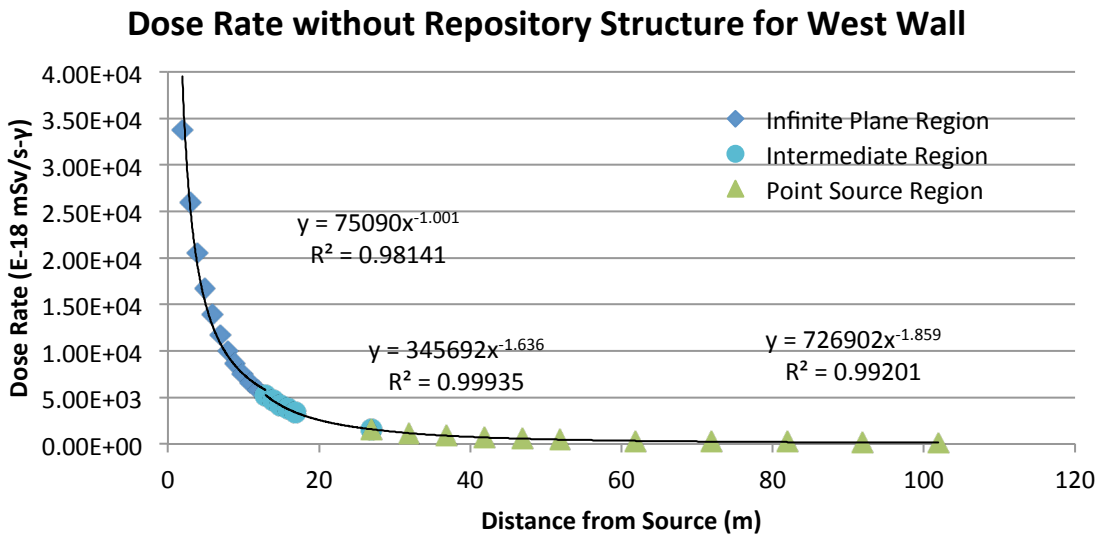

Figure 30 Dose Rate Profile Without Repository Structures for the West Wall

The following is a plot comparing the dose rate profile with and without the repository structure. A logarithmic scale is used on the abscissa.

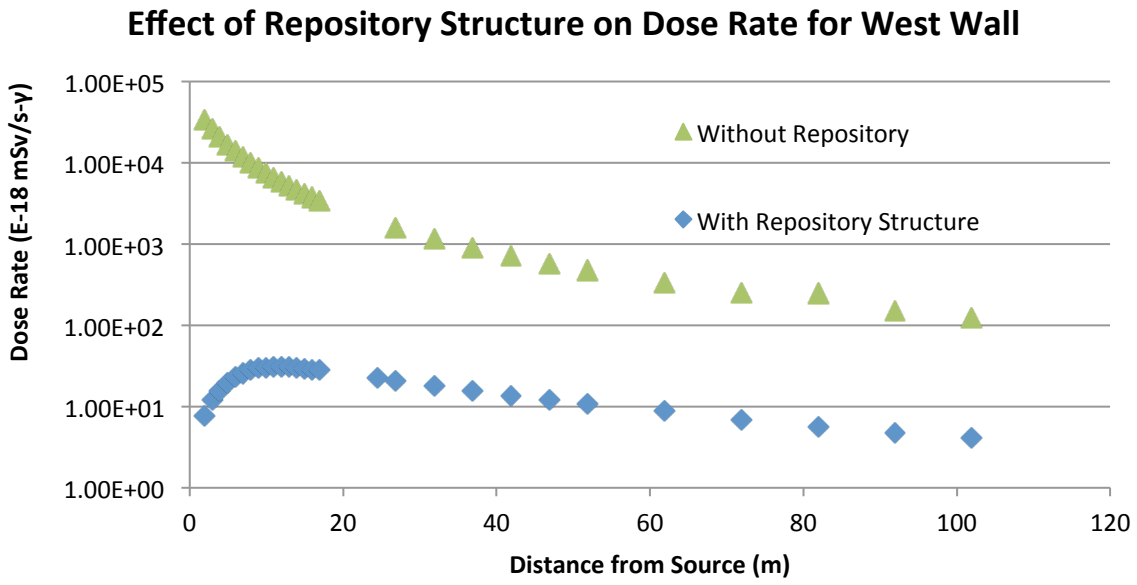

Figure 31 Dose Rate Profile With and Without Repository Structures for the West Wall

To ascertain the contribution that was not due to attenuation, the simulation without the repository structure was corrected for attenuation. When the curve without the repository is

corrected for attenuation, the plot with the repository rises above the curve without the repository structure.

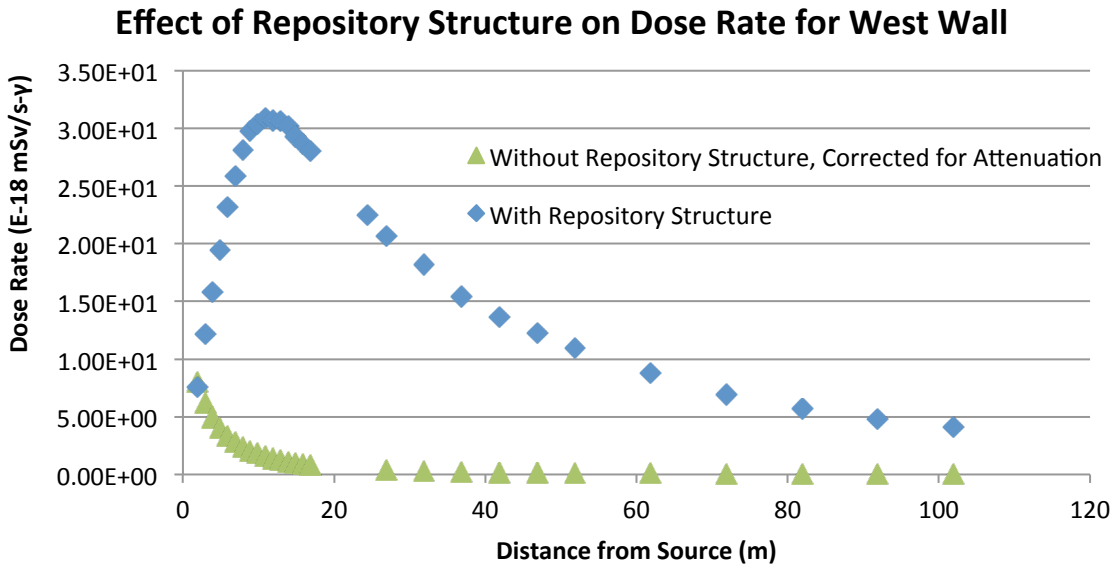

Figure 32 Dose Rate Profile With and Without Repository Structures (Corrected for Attenuation) for the West Wall

The contribution due to effects besides attenuation was derived by subtracting the attenuation corrected dose rate from the dose rate with the repository structure.

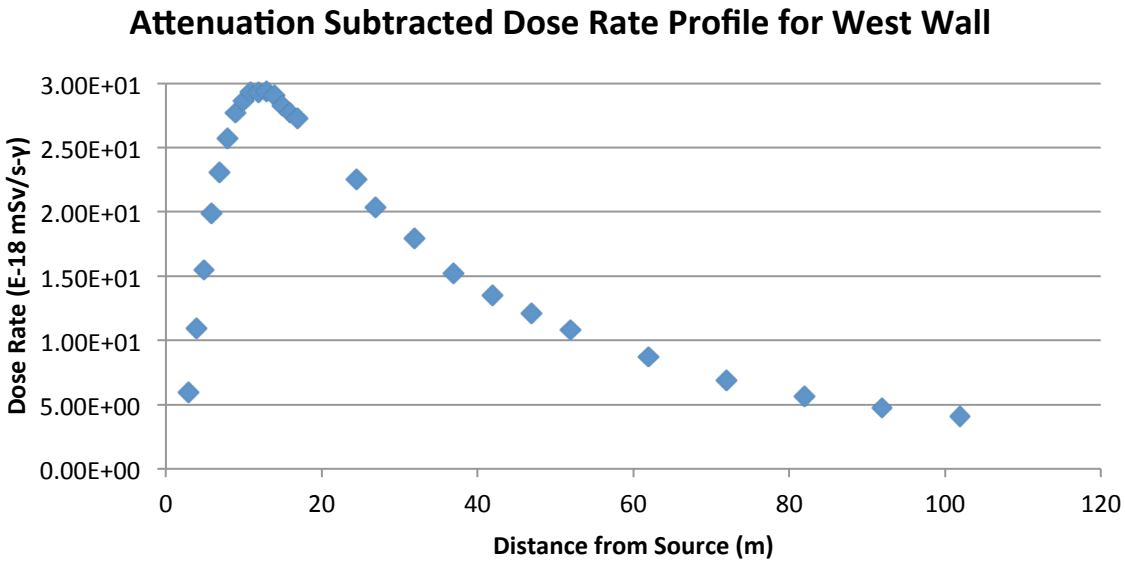

Figure 33 Non-Attenuation Contribution to Dose Rate Profile for North Side

South Wall

The dose rate profile for all heights was divided into two regions, as shown in Figure 19. Smooth analytic functions were fit to the regions corresponding to Equations 15 through 17. Fitting function information, including bounds of fitted regions and the R^2 value for the trendline, is presented in Table 12. Graphs used to derive the trendlines are presented in Appendix B. It should be noted that for the height of 5.21 m, dose rates were only evaluated up to 40.45 m from the front waste barrel row. The following is a table containing the fit information for the skyshine and wall effects regions for the south wall.

Table 12 Fit Information for the Infinite Plane & Point Source Regions for the South Wall

Height (m)	Infinite Plane				Point Source			
	Region (m)	A_3 (E-18 mSv/s-γ)	B_3	R^2	Region (m)	A_3 (E-18 mSv/s-γ)	B_3	R^2
1.465	0-25.45	7.61E3	0.921	0.993	25.45-105.45	1.98E5	1.91	0.994
2.605	0-30.45	1.28E4	1.10	0.995	30.45-105.45	2.44E5	1.96	0.995
3.745	0-20.45	1.32E4	1.09	0.999	30.45-105.45	2.49E5	1.96	0.996
4.4775	0-25.45	1.25E4	1.08	0.996	25.45-105.45	1.76E5	1.87	0.994
5.21	0-25.45	1.02E4	1.006	0.991	25.45-40.45	4.43E4	1.48	0999

The infinite plane and point source regions identified exhibit similar B_2 and B_3 values to the expected power values to 1 and 2 as described in Equations 13 and 14, respectively. To ascertain how closely the regions follow these hypothetical functions for the height of 3.745 m, the infinite plane and the point source regions were force fit to Equations 13 and 14, respectively. Only the height of 3.745 m was chosen, because for this height the infinite plane and point source regions could be identified individually. Equation 21 was derived for the infinite plane source region by optimizing D_0 based on the R^2 value.

$$y = \frac{10800}{x} \qquad \textbf{21}$$

The derived trendline (Equation 21) is plotted with fitted data in Figure 34. To determine the degree of fit for the trendline, the coefficient of determination (R^2) was calculated as 0.949.

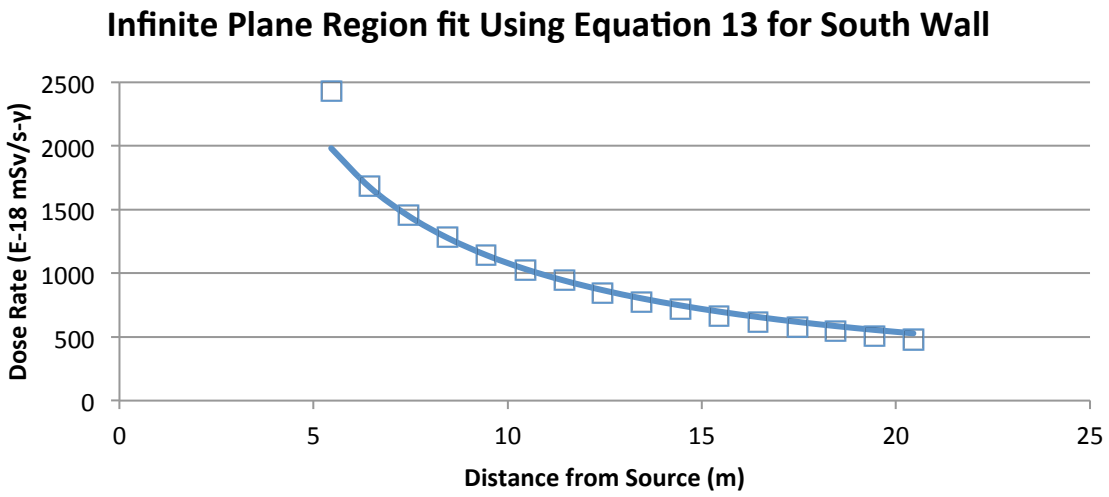

Figure 34 Infinite Plane Region Force Fit to Equation 13 for South Wall

Similarly, the equation for the point source region was derived by optimizing D_0 based on the R^2 value, and is shown in Equation 22.

$$y = \frac{260000}{x^2} \qquad \textbf{22}$$

The derived trendline (Equation 22) was plotted with the fitted data in Figure 35. The degree of fit for the trendline was determined by calculating R^2, which was calculated as 0.988.

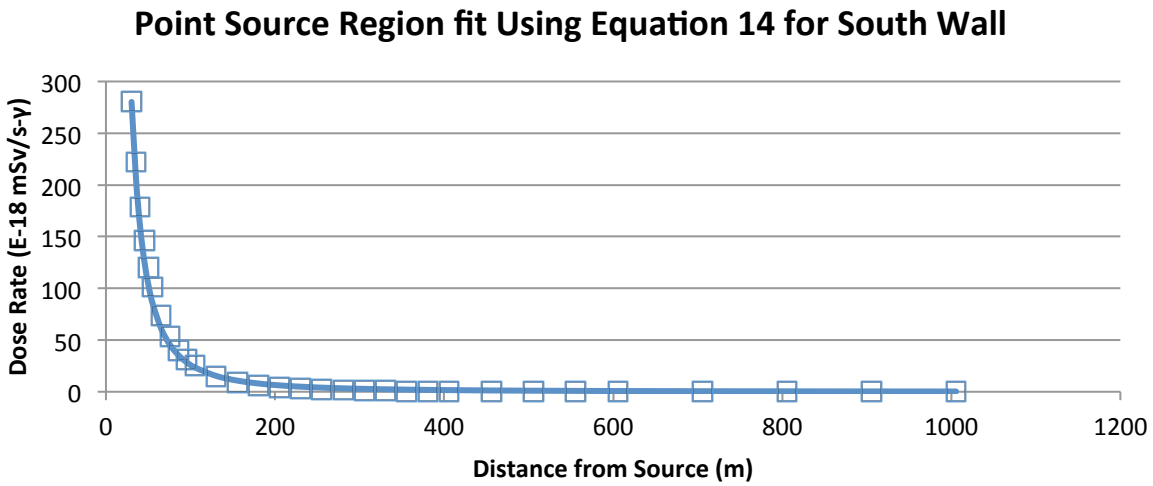

Figure 35 Point Source Region Force Fit to Equation 14 for North Wall

A plot of the dose rate profiles for the five heights is presented in Figure 36.

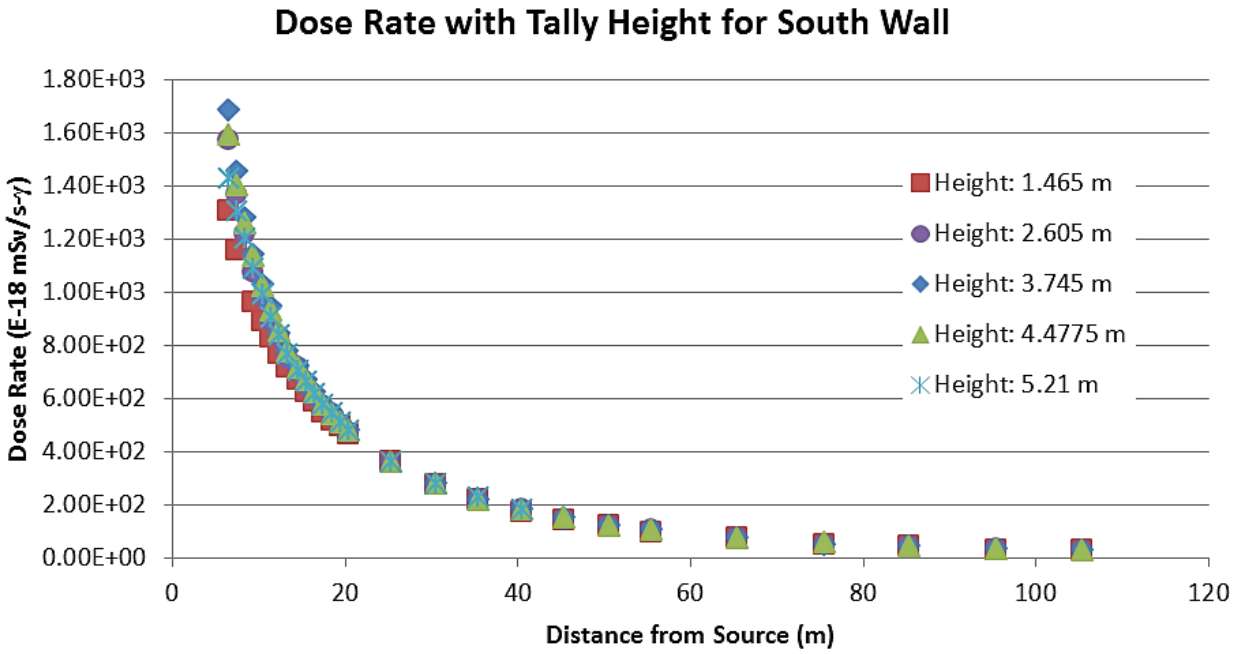

Figure 36 Dose Rate v. Distance for all Heights for the South Wall

The dose rate profile for the south wall was analyzed with and without the repository structure at a height of 3.745 m. The following is a graph of the dose rate with smooth analytic fit functions.

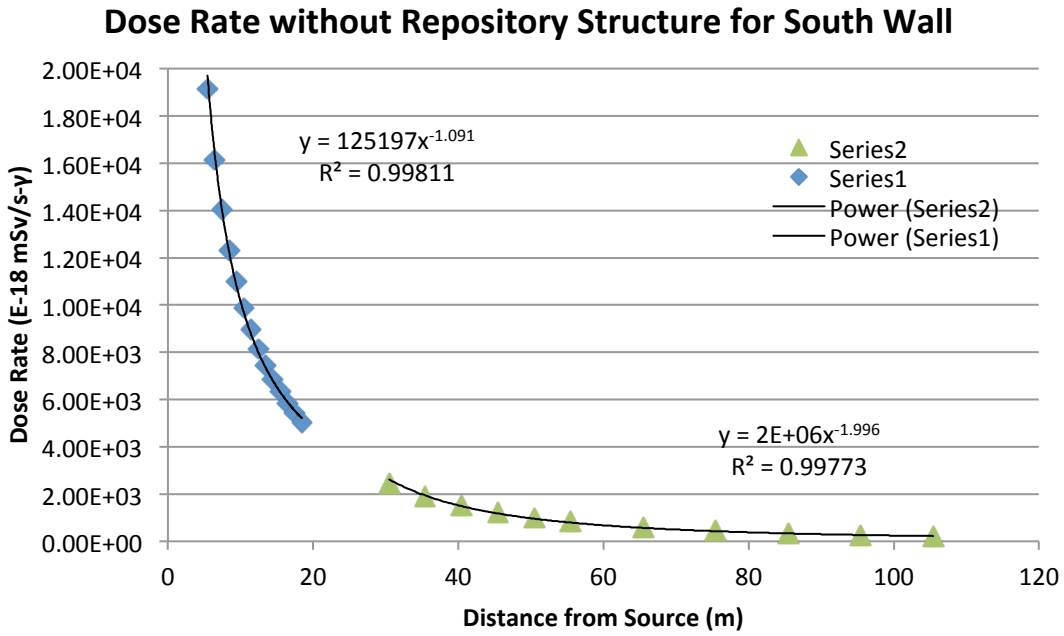

Figure 37 Dose Rate Profile Without Repository Structures for the South Wall

The following is a plot comparing the dose rate profile with and without the repository structure. A logarithmic scale is used on the abscissa.

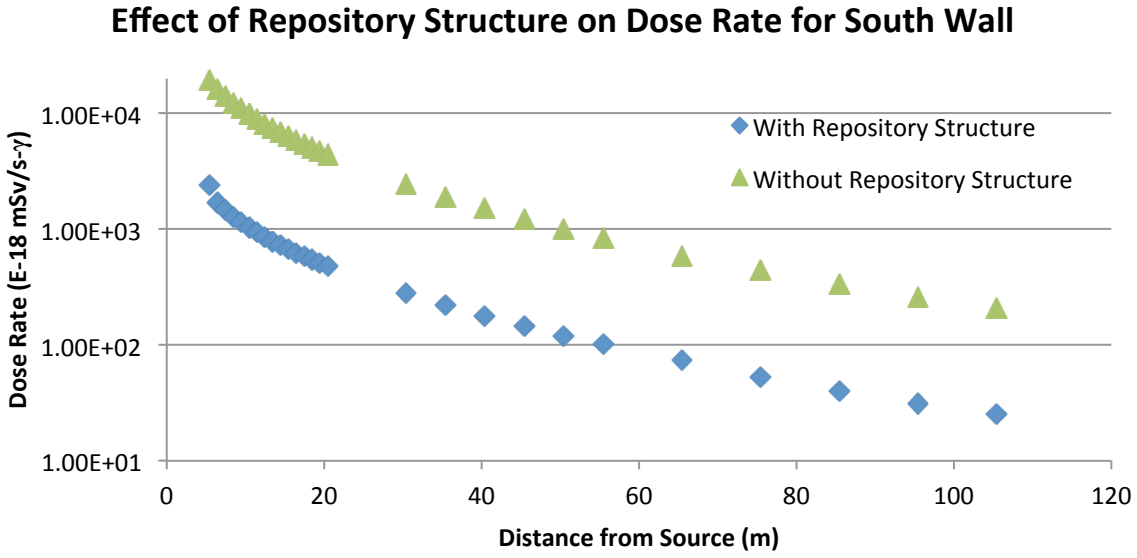

Figure 38 Dose Rate Profile With and Without Repository Structures for the South Wall

To ascertain the contribution that was not due to attenuation, the simulation without the repository structure was corrected for attenuation. When the curve without the repository is corrected for attenuation, the plot with the repository remains less than but very similar to the curve with the repository.

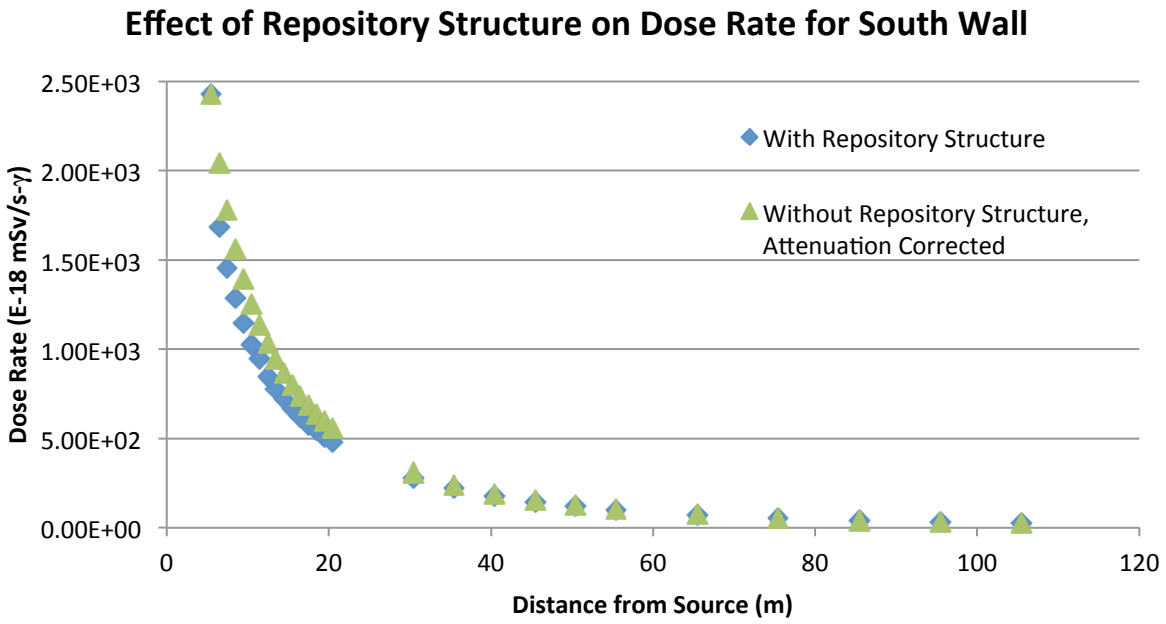

Figure 39 Dose Rate Profile With and Without Repository Structures (Attenuation Corrected) for the South Wall

The contribution due to effects besides attenuation was derived by subtracting the attenuation corrected dose rate without the repository structure from the dose rate with the repository structure.

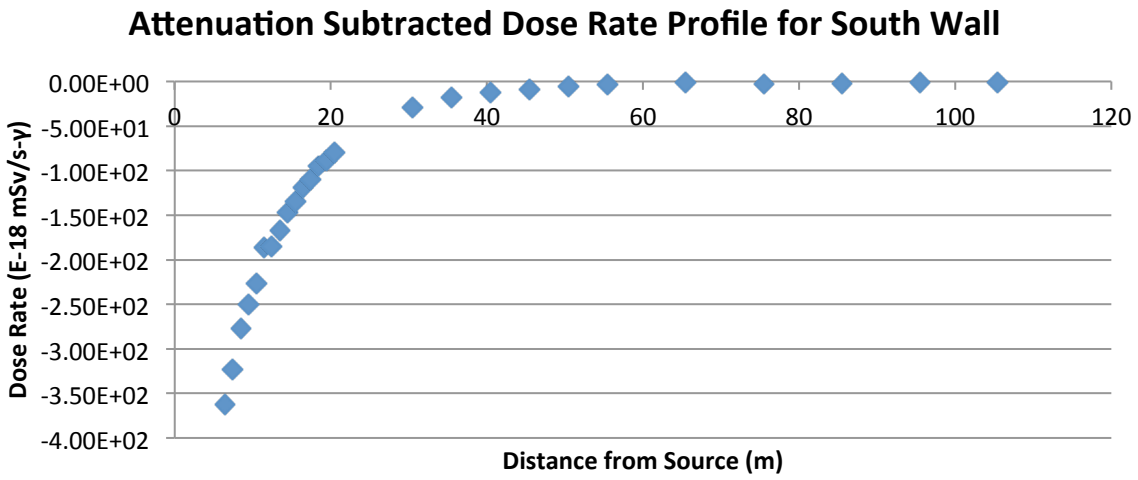

Figure 40 Non-Attenuation Contribution to Dose Rate Profile for South Side

DISCUSSION

Vertical Profiles

The vertical dose rate profiles evaluated for the north and west walls are similar, as shown in Figure 17. At first, the dose rate increases approximately linearly from a vertical distance of 1.5 m to 6 m, corresponding to the vertical location of the drum set. At heights past 6 m, the dose rate increases more rapidly. The observations in Figure 17 are inconsistent with our hypothesis; it was hypothesized that only the first row of drums would contribute significantly and a maximum would be reached at the midpoint of the drum set. The lack of a maximum and the continued increase of the dose rate suggests that further rows of the drum source provide additional contributions to the total dose rate. When the dose rate measurements are directly in front of the drum source, it is likely that only the first rows of the drums provide the main contribution as a source. However, as the height continues to increase, the drums behind the front columns become more significant as a source. Finally, after the top of the drum set is reached, the tops of the drum stacks begin to influence the dose rate by acting as additional sources. The tops of the drum stacks contribute more significantly to dose than previously expected.

At lower elevations, the dose rate for the north wall is consistently lower than for the west side until a height of approximately 7.5 m above the ground. This could be due to the lateral dimensions of the source present at both locations (Figure 14). The north lateral dimension of the source is approximately 2.5 times the west lateral dimension of the source.

Horizontal Profiles

The typical dose rate profile for the west and north walls (Figure 18) exhibits a peak and subsequent decrease, while the south side exhibits a constant decrease (Figure 19). It was

expected that the dose profile for all sides would exhibit a constant decrease with two main sections with analytic functions corresponding to an infinite plane and a point source. These two main sections exist for the profile for the south side, but do not characterize the entire profile for the north and west sides. The main differences between the north/west sides and the south side include the lack of shielding on the south side and the presence of a larger gap between the entire drum source and the wall (Figure 14). The discrepancy between the expected and observed results for the north and west sides possibly could be explained by wall effects through the shielding or by skyshine.

Four sections were identified for the north and west sides corresponding to: skyshine and wall effects region characterized by a logarithmic increase (Equation 13) and an exponential decrease (Equation 14), infinite plane region (Equation 15), and point source region (Equation 15). The dose rate profiles were also evaluated for the north and west sides without the repository structure (walls and roof) shown in Figure 26 and Figure 32, respectively. When the repository structure was not present, the initial peak dose rate was not observed. The lack of a peak without the repository structures suggests that the peak is the result of the repository structures through either skyshine or scattering through the walls of the repository.

The shape of the north and west wall dose rate profiles follows closely to the profiles developed by Elder and McGinley for accelerator skyshine (Figure 8) [18] [19]. Skyshine was analyzed for the Varian Trilogy Linear Accelerator at the Colorado State University Veterinary Medical Center [18] and for Varian 2100 C Treatment Rooms [19]. Both works found an initial increase in photon dose rate, peaking around 300% of the original dose rate, and returning to the original dose rate at around 30 m (Figure 8). Similarly, in this work the peak reached between 250% and 300% of the original dose rate value, depending on the vertical height; however, dose

rates did not return to the original value until around 65 m from the source (Figure 22 and Figure 28).

The peak in the north and west wall dose rate profiles was further analyzed by taking the dose rate profile at various heights for the north, west, and south sides. For the initial rise in the profiles of the north and west walls, the constant A_1 in the logarithmic function increases with vertical height (Table 8 and Table 10), indicating that a steeper logarithmic rise occurs, as shown in Figure 22 and Figure 28. Additionally for the exponential decrease region, the constants A_2 and B_2 increase (Table 8 and Table 10) indicating a larger maximum dose rate and quicker decrease, as shown in Figure 22 and Figure 28. For the south side, the changes in height do not strongly affect the dose rate functions, as shown in Figure 36.

For the north and west wall profiles, the variation of peak location with tally height was investigated. As the tally height increases the peak occurs closer to the source. The relationship between peak location and tally height closely followed a linear relationship. The differences in the peak location with vertical height, steeper rise in dose rate, and more rapid decrease in dose rate suggest an influence of the scattering angle in either the air or repository material on the dose rate profile. For a certain angle, the projected straight-line path of the photons will pass closer to the repository for more elevated points (see Figure 7). If the dose rate is due to skyshine, the scattering will be limited to the vertical region above the waste repository subtended by the source and the dose rate near the repository will be limited as the height above the repository decreases.

CONCLUSIONS

The dose rate profiles developed for the north side of the repository closely follow the dose rates observed due to skyshine as reported and measured by Elder and McGinley for medical accelerator facilities. As detector tally height increases, the dose rate increases more rapidly and reaches a larger maximum. A higher maximum dose rate at greater heights could be due to greater intensity of radiation, more energetic radiation, or a combination of both, while the more rapid increase could be due to the angle of scattering due to skyshine, reaching the detector position. The lack of maxima in the south side profile, suggests that the larger air gap or smaller wall thickness affects skyshine or effects seen due to wall effects.

The observed maxima are between 250% and 300% of the original dose rate for the north and west sides, and the dose rate does not decrease to the original dose rate (dose rate at repository wall) until around 65 m from the front waste barrel row. The increase in dose rate is significant. Current waste repository designs, do not consider skyshine or scattering in repository material. This work suggests that skyshine and scattering are significant and should be considered.

Future work would include further source manipulation to determine more precisely if the observed effects are due to skyshine or scattering in the repository material. This could be achieved by changing the roof material, thickness, or pitch, or by adding a void region.

REFERENCES

[1] U.S. Nuclear Regulatory Commission, "Radioactive Waste: Production, Storage, Disposal (NUREG/BR-0216, Rev. 2)," U.S. Nuclear Regulatory Commission, Washington, 2002.

[2] H. Cember and T. E. Johnson, Introduction to Health Physics, McGraw-Hill Companies, Inc, 2009.

[3] International Atomic Energy Agency, "Management of Radioactive Waste from the Use of Radionuclides in Medicine (IAEA-TECDOC-1183)," International Atomic Energy Agency, Vienna, 2000.

[4] International Atomic Energy Agency, "Radiation Safety in Industrial Radiography," International Atomic Energy Agency Specific Safety Guide, Vienna, 2011.

[5] KAERI, "27-cobalt-59," KAERI, [Online]. Available: http://atom.kaeri.re.kr/ton/nuc9.html. [Accessed 1 October 2013].

[6] KAERI, "27-cobalt-60," KAERI, [Online]. Available: http://atom.kaeri.re.kr/ton/nuc9.html. [Accessed 1 October 2013].

[7] International Atomic Energy Agency, "Classification of Radioactive Waste (No. GSG-1)," International Atomic Energy Agency, Vienna, 2009.

[8] R. A. Knief, Nuclear Engineering: Theory and Technology of Nuclear Power, La Grange

Park: American Nuclear Society, 2008.

[9] U.S. Nuclear Regulatory Commission, "Title 10, Code of Federal Regulations," U.S. Nuclear Regulatory Commission, Washington, 2013.

[10] NAC International, INC, "NAC Multi-Purpose Canister (NAC-MPC) Sytem Safety Evaluation Report," NRC, 2004.

[11] T. E. Johnson and B. K. Birky, Health Physics and Radiological Health, Baltimore: Lippincott Williams & Wilkins, 2012.

[12] J. J. Bevelacqua, "Point Source Approximations in Health Physics," *Radiation Protection Management,* vol. 21, no. 5, pp. 9-13, 2004.

[13] N. Zoeger and A. Brandl, "Dose Rate Distribution from a Standard Waste Drum Arrangement," *Health Physics,* pp. S142-S147, 2011.

[14] J. Shultis and R. Faw, Radiation Shielding, La Grange Park: American Nuclear Society, Inc., 2000.

[15] J. Turner, Atoms, Radiation, and Radiation Protection, Weinheim: Wiley-VCH, 2009.

[16] J. Hubbell and S. Seltzer, "Tables of X-Ray Mass Attenuation Coefficients and Mass Energy-Absorption Coefficients from 1 keV to 20 MeV for Elements Z = 1 to 92 and 48 Additional Substances of Dosimetric Interest*," NIST Standard Reference Database 126, Gaithersburg, 1996.

[17] R. Brockhoff and J. Shultis, "Data for the Calculation of Albedos from Concrete, Iron, Lead,

and Water for Photons and Neutrons," Engineering Experimental Station, Manhattan, 2005.

[18] D. E. Elder, "Skyshine Radiation Resulting from 6 MV and 10 MV Photon Beams From a Medical Accelerator," Colorado State University, Fort Collins, 2008.

[19] P. H. McGinley, "Radiation Skyshine Produced by an 18 MeV Medical Accelerator," *Radiation Protection Management,* vol. 10, no. 5, pp. 59-64, 1993.

[20] X-5 Monte Carlo Team, "Volume I: Overview and Theory," in *MCNP - A General Monte Carlo N-Particle Transport Code*, Los Alamos, Los Alamos National Laboratory, 2008.

[21] J. K. Shultis and R. E. Faw, An MCNP Primer, Manhattan: Kansas State University, 2006.

[22] A. Schwarz, R. Schwarz and L. Carter, "MCNP/MCNPX Visual Editor Computer Code," 2008.

[23] International Commission on Radiological Protection, "ICRP Publication 21," *Recommendations of the International Commission on Radiation Protection,* no. 21, 1973.

[24] R. H. Thomas, "The History and Future of Accelerator Radiological Protection," *Radiation Protection Dosimetry,* vol. 96, no. 4, pp. 441-457, 2001.

[25] MCNPX Team, "Monte Carlo N-Particle eXtended," Los Alamos National Laboratory, Los Alamos, 2008.

[26] I. Lagutina, V. P. Mashkovich, A. Stroganov and A. Chernyaev, "Skyshine From Photon Radiation," Plenum Publishing Corporation, 1989, pp. 118-124.

APPENDIX A

Sample Input Deck for Waste Repository

Complete Repository

Waste Repository Model

c Cell Card Definitions

c 4 Drum Lattice (1-20)

```
1   0 -41 fill=2 imp:p=1                $Lattice universe
2   0 -40 u=2 imp:p=1 lat=1 fill=0:20 0:16 0:6 1 2498r   $Lattice element
3   1 -1.124e-3 41 -999 #20 #21 #22 #24 #25 #26 #27
    #28 #29 #30 #31 #40 imp:p=1    $Outside lattice
4   1 -1.124e-3 42 45 48 51 u=1 imp:p=1     $Air space around Barrels
5   2 -7.87 -42 43 44 u=1 imp:p=1          $Barrel 1 steel wall
6   3 -2.3 -43 u=1 imp:p=1               $Barrel 1 concrete
7   1 -1.124e-3 -44 u=1 imp:p=1           $Barrel 1 air space
8   2 -7.87 -45 46 47 u=1 imp:p=1          $Barrel 2 steel wall
9   3 -2.3 -46 u=1 imp:p=1               $Barrel 2 concrete
10  1 -1.124e-3 -47 u=1 imp:p=1           $Barrel 2 air space
11  2 -7.87 -48 49 50 u=1 imp:p=1          $Barrel 3 steel wall
12  3 -2.3 -49 u=1 imp:p=1               $Barrel 3 concrete
13  1 -1.124e-3 -50 u=1 imp:p=1           $Barrel 3 air space
14  2 -7.87 -51 52 53 u=1 imp:p=1          $Barrel 4 steel wall
15  3 -2.3 -52 u=1 imp:p=1               $Barrel 4 concrete
16  1 -1.124e-3 -53 u=1 imp:p=1           $Barrel 4 air space
c Building (20-40)
20  3 -2.2 -1 2 imp:p=1                 $Building walls
```

```
21  3 -2.2 -3 imp:p=1                $Shielding (NO)
22  3 -2.2 -4 imp:p=1                $Shielding (SO)
24  3 -2.2 -6 imp:p=1                $Shielding (SW)
25  3 -2.2 -7 imp:p=1                $Foundation
26  3 -2.2 -22 -21 20 imp:p=1          $Left Roof
27  3 -2.2 -25 -24 23 imp:p=1          $Right Roof
28  3 -2.2 -26 -20 imp:p=1           $Near Left Side
29  3 -2.2 -27 -23 imp:p=1           $Near Right Side
30  3 -2.2 -28 -20 imp:p=1           $Far Left Side
31  3 -2.2 -29 -23 imp:p=1           $Far Right Side
c Ground
40 3 -1.2 -999 -8 imp:p=1
c Void
999 0 999 imp:p=0                    $Void


c Surface Card Definitions
c Building Dimensions (1-50)
1 BOX -286.6 -544.7 -97.5  6133.2 0 0  0 3006.9 0  0 0 831 $Building ext.
2 BOX -266.6 -524.7 -52.5  6093.2 0 0  0 2966.9 0  0 0 786 $Building interior
3 BOX -266.6 -524.7 -52.5  70 0 0  0 2896.9 0  0 0 786 $Shielding (NO)
4 BOX -266.6 2372.2 -52.5  6093.2 0 0  0 70 0  0 0 786 $Shielding (SO)
6 BOX 5756.6 2372.2 -52.5  70 0 0  0 -2896.9 0  0 0 786 $Shielding (SW)
7 BOX -286.6 -544.7 -146.5  6388.2 0 0  0 3006.9 0  0 0 49 $Foundation
```

8 PZ -146.5 $Ground

c Roof

20 P -286.6 -544.7 733.5 -286.6 958.75 955.5 5846.6 -544.7 733.5 $Lower L

21 P -286.6 -544.7 753.5 -286.6 958.75 975.5 5846.6 -544.7 753.5 $Upper L

22 BOX -286.6 -544.7 733.5 6133.2 0 0 0 1503.45 0 0 0 242 $Box containing L

23 P -286.6 2462.2 733.5 -286.6 958.75 955.5 5846.6 2462.2 733.5 $Lower R

24 P -286.6 2462.2 753.5 -286.6 958.75 975.5 5846.6 2462.2 753.5 $Upper R

25 BOX -286.6 958.75 733.5 6133.2 0 0 0 1503.45 0 0 0 242 $Box containing R

26 BOX -286.6 -544.7 733.5 20 0 0 0 1503.42 0 0 0 222 $Near Left Side wall

27 BOX -286.6 958.75 733.5 20 0 0 0 1503.42 0 0 0 222 $Near Right Side wall

28 BOX 5826.6 -544.7 733.5 20 0 0 0 1503.42 0 0 0 222 $Near Left Side wall

29 BOX 5826.6 958.75 733.5 20 0 0 0 1503.42 0 0 0 222 $Near Right Side wall

c Lattice Elements (40-60)

40 BOX -141.1 -99.55 -38 278.2 0 0 0 134.8 0 0 0 76 $Lattice element

41 BOX -141.1 -99.55 -38 5842.2 0 0 0 2291.6 0 0 0 532 $Lattice universe

42 RCC -4 0 0 -92.6 0 0 28.15 $Barrel 1 steel wall

43 RCC -4.5 0 0 -85.6 0 0 28 $Barrel 1 concrete

44 RCC -90.1 0 0 -6.2 0 0 28 $Barrel 1 air space

45 RCC 0 0 0 92.6 0 0 28.15 $Barrel 2 steel wall

46 RCC 0.5 0 0 85.6 0 0 28 $Barrel 2 concrete

47 RCC 86.1 0 0 6.2 0 0 28 $Barrel 2 air space

48 RCC -4 -64.3 0 -92.6 0 0 28.15 $Barrel 3 steel wall

49 RCC -4.5 -64.3 0 -85.6 0 0 28 $Barrel 3 concrete

```
50  RCC -90.1 -64.3 0 -6.2 0 0 28          $Barrel 3 air space
51  RCC 0 -64.3 0 92.6 0 0 28.15           $Barrel 4 steel wall
52  RCC 0.5 -64.3 0 85.6 0 0 28            $Barrel 4 concrete
53  RCC 86.1 -64.3 0 6.2 0 0 28            $Barrel 4 air space
c Universe
999 SO 20000                               $Universe


c Material Cards, Source Cards, Tallies
mode p
c Materials
m1   6000   -.000125   $Comp of dry air (NIST)
     7000   -.755267
     8000   -.231781
     18000  -.012827
m2   26000  1.0        $Natural iron
     gas=0
m3   1001   0.1170     $Concrete
     8016   0.6082
     14000  0.2748
     gas=0
c Source (Sampling Cylinder Method)
sdef pos=fcel=d7 par=2 rad=d1 cel=d2 ext=d8 axs=1 0 0 erg=d9
si1  0 28           $Radius of concrete
```

```
sp1  -21 1          $Weighting for radial sample, r^1
si2  s d3 d4 d5 d6   $Specifies chosen cells
sp2  1 1 1 1        $Probability distribution between cells
si3  L 1:2:6        $Barrel 1
sp3  1              $Probability distribution for center of barrel 1
si4  L 1:2:9        $Barrel 2
sp4  1              $Probability distribution for center of barrel 2
si5  L 1:2:12       $Barrel 3
sp5  1              $Probability distribution for center of barrel 3
si6  L 1:2:15       $Barrel 4
sp6  1              $Probability distribution for center of barrel 4
ds7  L -90.1 0 0 0.5 0 0 -90.1 -64.3 0 0.5 -64.3 0 $Center of drums
si8  h 0 85.6       $Extends length of concrete region
sp8  -21 0          $Weighting for axial sample, 0
si9  L 1.173 1.332   $Energies for Co-60
sp9  d 0.5 0.5      $Distribution for Energies of Co-60
c Tallies (ICRP-21)
c Left
f5:p -12786.6 958.75 228 1  $ 12500 cm
de5 log 0.01 0.015 0.02 0.03 0.04 0.05 0.06 0.08 &
    0.1 0.15 0.2 0.3 0.4 0.5 0.6 0.8 1 1.5 2
df5 log 2.78E-6 1.11E-6 5.88E-7 2.56E-7 1.56E-7 1.20E-7 1.11E-7 1.20E-7 &
    1.47E-7 2.38E-7 3.45E-7 5.56E-7 7.69E-7 9.09E-7 1.14E-6 1.47E-6 &
```

1.79E-6 2.44E-6 3.03E-6

nps 5e8

Print

Repository without Walls

Waste Repository Model

c Cell Card Definitions

c 4 Drum Lattice (1-20)

1 0 -41 fill=2 imp:p=1 $Lattice universe

2 0 -40 u=2 imp:p=1 lat=1 fill=0:20 0:16 0:6 1 2498r $Lattice element

3 1 -1.124e-3 41 -999 #40 imp:p=1 $Outside lattice

4 1 -1.124e-3 42 45 48 51 u=1 imp:p=1 $Air space around Barrels

5 2 -7.87 -42 43 44 u=1 imp:p=1 $Barrel 1 steel wall

6 3 -2.3 -43 u=1 imp:p=1 $Barrel 1 concrete

7 1 -1.124e-3 -44 u=1 imp:p=1 $Barrel 1 air space

8 2 -7.87 -45 46 47 u=1 imp:p=1 $Barrel 2 steel wall

9 3 -2.3 -46 u=1 imp:p=1 $Barrel 2 concrete

10 1 -1.124e-3 -47 u=1 imp:p=1 $Barrel 2 air space

11 2 -7.87 -48 49 50 u=1 imp:p=1 $Barrel 3 steel wall

12 3 -2.3 -49 u=1 imp:p=1 $Barrel 3 concrete

13 1 -1.124e-3 -50 u=1 imp:p=1 $Barrel 3 air space

14 2 -7.87 -51 52 53 u=1 imp:p=1 $Barrel 4 steel wall

15 3 -2.3 -52 u=1 imp:p=1 $Barrel 4 concrete

16 1 -1.124e-3 -53 u=1 imp:p=1 $Barrel 4 air space

c Ground

40 3 -1.2 -999 -8 imp:p=1

c Void

```
999 0 999 imp:p=0                    $Void


c Surface Card Definitions
c Building Dimensions (1-50)
8 PZ -146.5 $Ground
c Lattice Elements (40-60)
40  BOX -141.1 -99.55 -38  278.2 0 0  0 134.8 0  0 0 76   $Lattice element
41  BOX -141.1 -99.55 -38  5842.2 0 0  0 2291.6 0  0 0 532 $Lattice universe
42  RCC -4 0 0 -92.6 0 0 28.15          $Barrel 1 steel wall
43  RCC -4.5 0 0 -85.6 0 0 28           $Barrel 1 concrete
44  RCC -90.1 0 0 -6.2 0 0 28           $Barrel 1 air space
45  RCC 0 0 0 92.6 0 0 28.15            $Barrel 2 steel wall
46  RCC 0.5 0 0 85.6 0 0 28             $Barrel 2 concrete
47  RCC 86.1 0 0 6.2 0 0 28             $Barrel 2 air space
48  RCC -4 -64.3 0 -92.6 0 0 28.15      $Barrel 3 steel wall
49  RCC -4.5 -64.3 0 -85.6 0 0 28       $Barrel 3 concrete
50  RCC -90.1 -64.3 0 -6.2 0 0 28       $Barrel 3 air space
51  RCC 0 -64.3 0 92.6 0 0 28.15        $Barrel 4 steel wall
52  RCC 0.5 -64.3 0 85.6 0 0 28         $Barrel 4 concrete
53  RCC 86.1 -64.3 0 6.2 0 0 28         $Barrel 4 air space
c Universe
999 SO 20000                         $Universe
```

```
c Material Cards, Source Cards, Tallies
mode p
c Materials
m1   6000   -.000125   $Comp of dry air (NIST)
     7000   -.755267
     8000   -.231781
     18000  -.012827
m2   26000  1.0        $Natural iron
     gas=0
m3   1001   0.1170     $Concrete
     8016   0.6082
     14000  0.2748
     gas=0
c Source (Sampling Cylinder Method)
sdef pos=fcel=d7 par=2 rad=d1 cel=d2 ext=d8 axs=1 0 0 erg=d9
si1  0 28            $Radius of concrete
sp1  -21 1           $Weighting for radial sample, r^1
si2  s d3 d4 d5 d6   $Specifies chosen cells
sp2  1 1 1 1         $Probability distribution between cells
si3  L 1:2:6         $Barrel 1
sp3  1               $Probability distribution for center of barrel 1
si4  L 1:2:9         $Barrel 2
sp4  1               $Probability distribution for center of barrel 2
```

```
si5  L 1:2:12        $Barrel 3
sp5  1               $Probability distribution for center of barrel 3
si6  L 1:2:15        $Barrel 4
sp6  1               $Probability distribution for center of barrel 4
ds7  L -90.1 0 0 0.5 0 0 -90.1 -64.3 0 0.5 -64.3 0 $Center of drums
si8  h 0 85.6        $Extends length of concrete region
sp8  -21 0           $Weighting for axial sample, 0
si9  L 1.173 1.332   $Energies for Co-60
sp9  d 0.5 0.5       $Distribution for Energies of Co-60
c Tallies (ICRP-21)
c Dose Profile (Bottom)
f5:p 2780 -544.7 228 1  $ 0 cm
de5 log 0.01 0.015 0.02 0.03 0.04 0.05 0.06 0.08 &
    0.1 0.15 0.2 0.3 0.4 0.5 0.6 0.8 1 1.5 2
df5 log 2.78E-6 1.11E-6 5.88E-7 2.56E-7 1.56E-7 1.20E-7 1.11E-7 1.20E-7 &
    1.47E-7 2.38E-7 3.45E-7 5.56E-7 7.69E-7 9.09E-7 1.14E-6 1.47E-6 &
    1.79E-6 2.44E-6 3.03E-6
nps 4e8
Print
```

APPENDIX B

Fitted Dose Rate Profile Plots

North Side

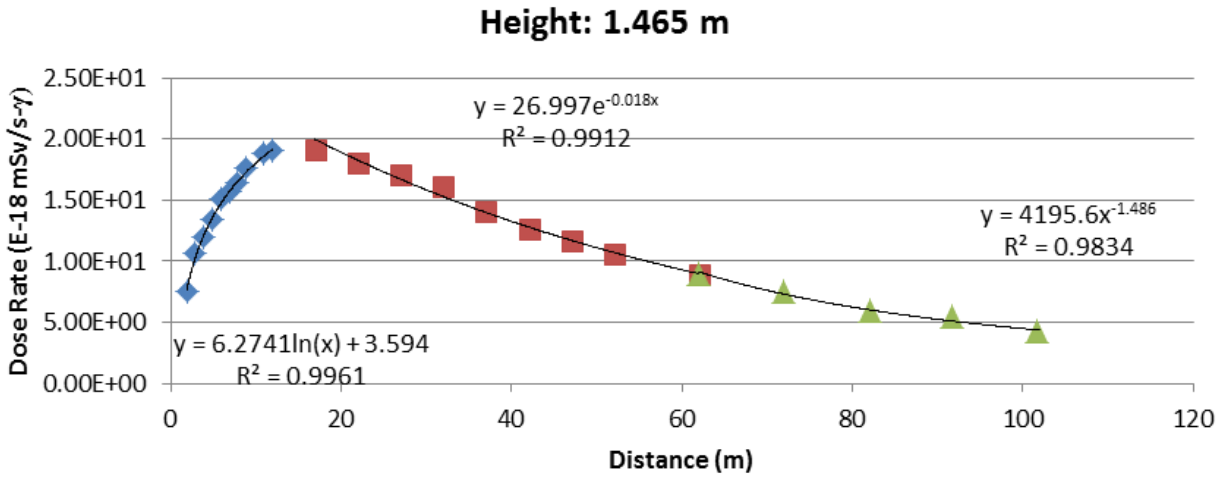

Figure 41 Fitted Dose Rate Profile for North Side at a Height of 1.465 m

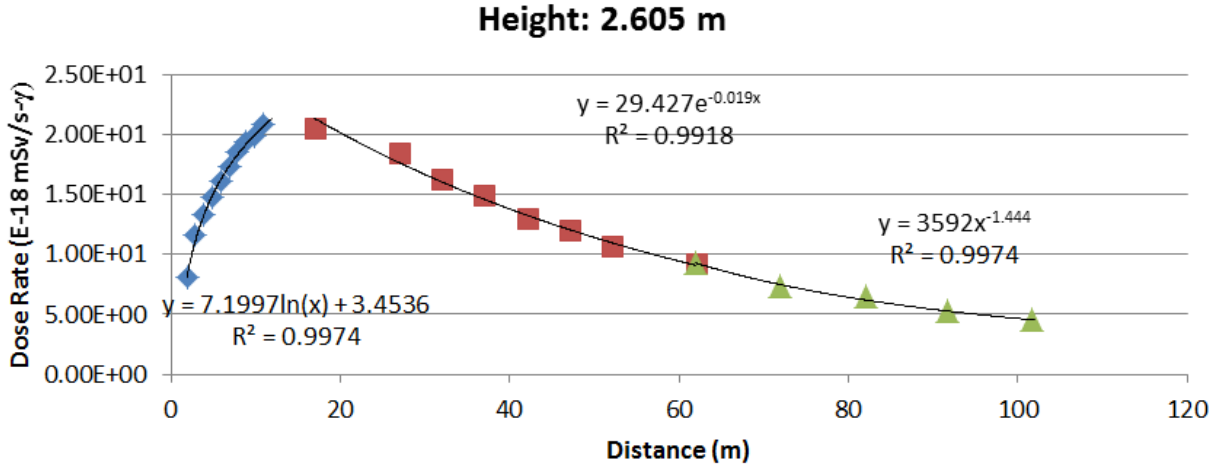

Figure 42 Fitted Dose Rate Profile for North Side at a Height of 2.605 m

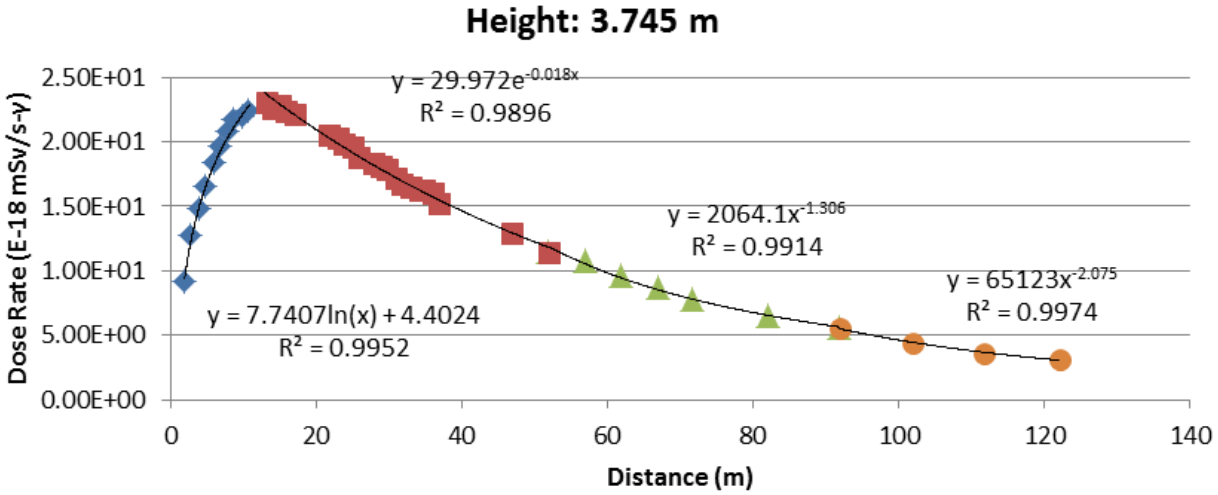

Figure 43 Fitted Dose Rate Profile for North Side at a Height of 3.745 m

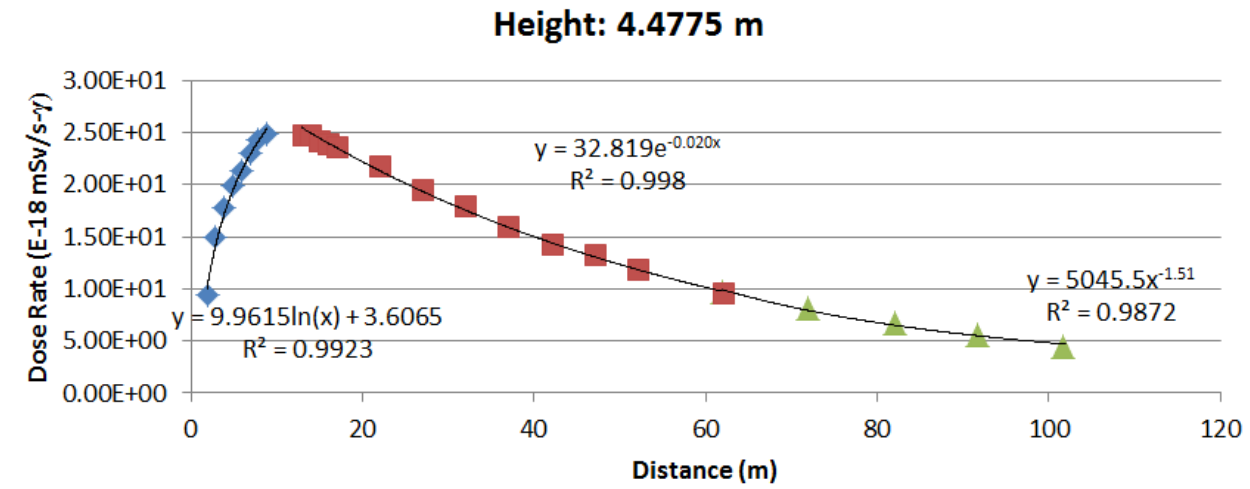

Figure 44 Fitted Dose Rate Profile for North Side at a Height of 4.4775 m

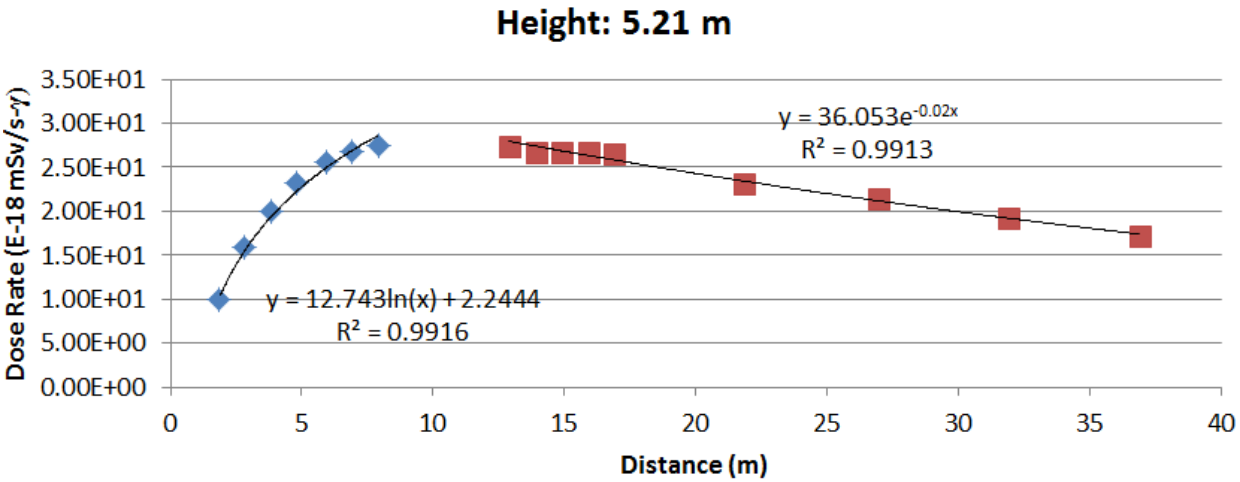

Figure 45 Fitted Dose Rate Profile for North Side at a Height of 5.21 m

West Side

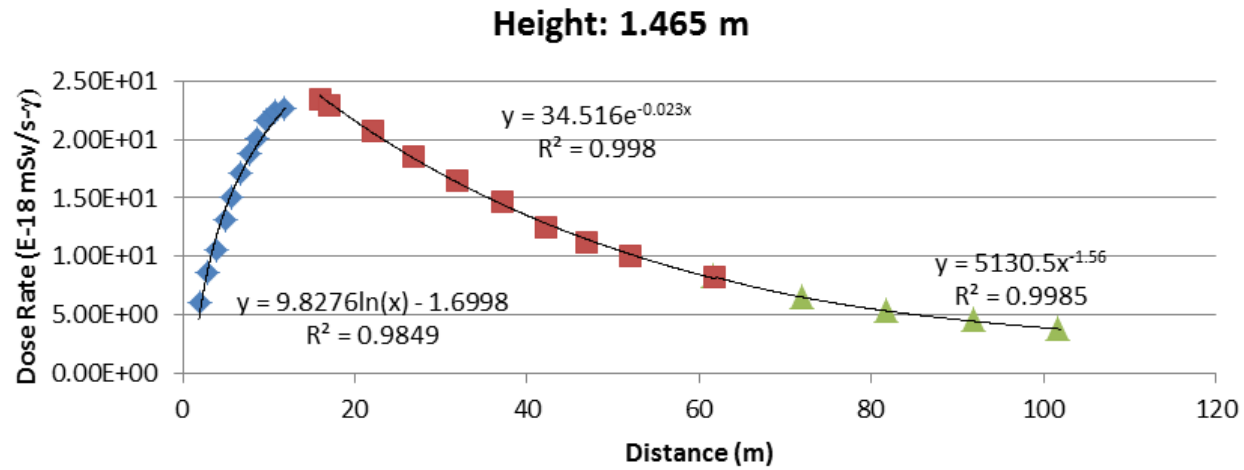

Figure 46 Fitted Dose Rate Profile for West Side at a Height of 1.465 m

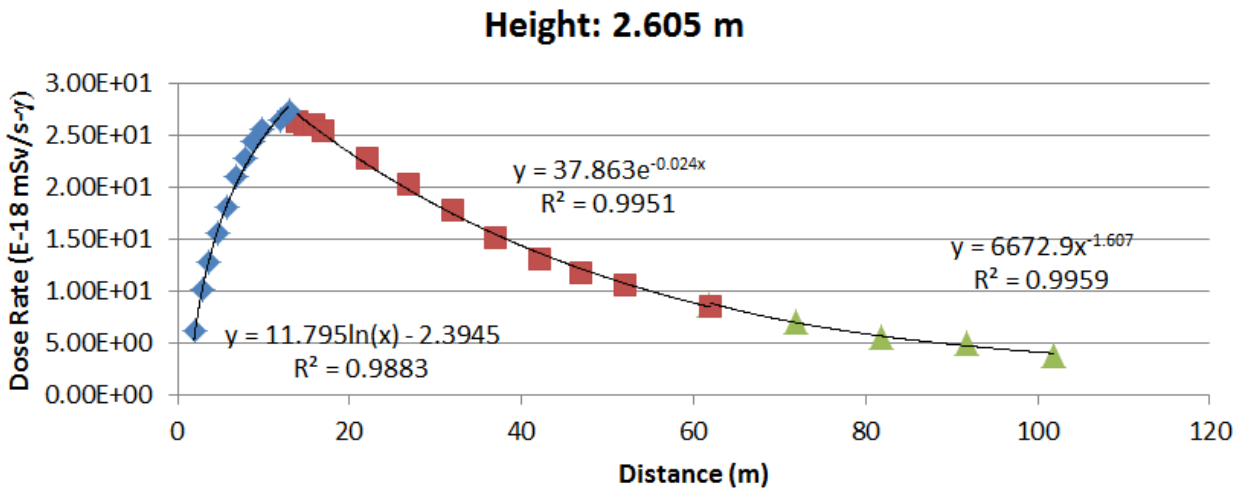

Figure 47 Fitted Dose Rate Profile for West Side at a Height of 2.605 m

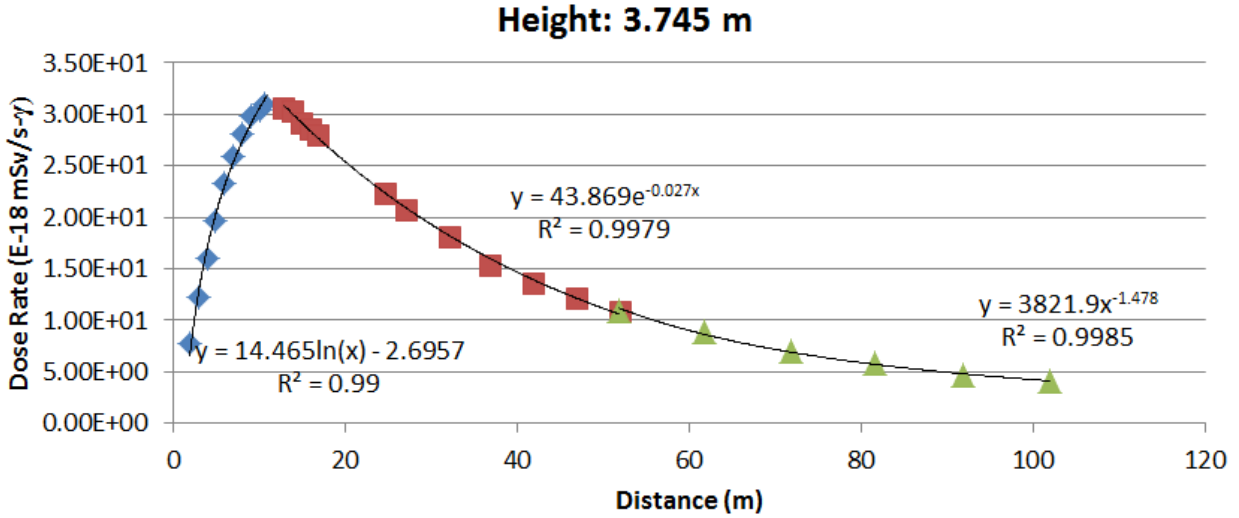

Figure 48 Fitted Dose Rate Profile for West Side at a Height of 3.745 m

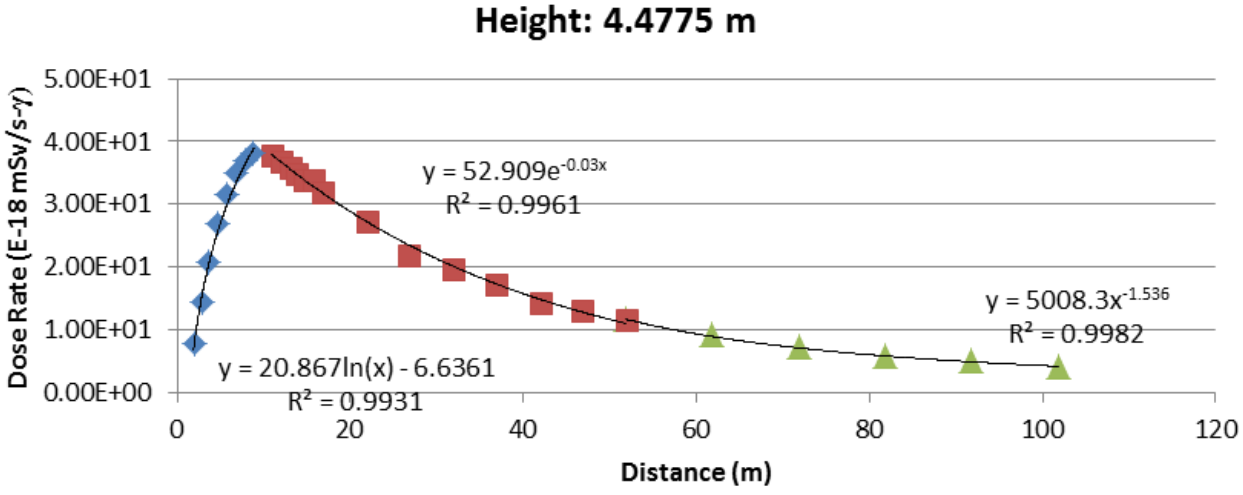

Figure 49 Fitted Dose Rate Profile for West Side at a Height of 4.4775 m

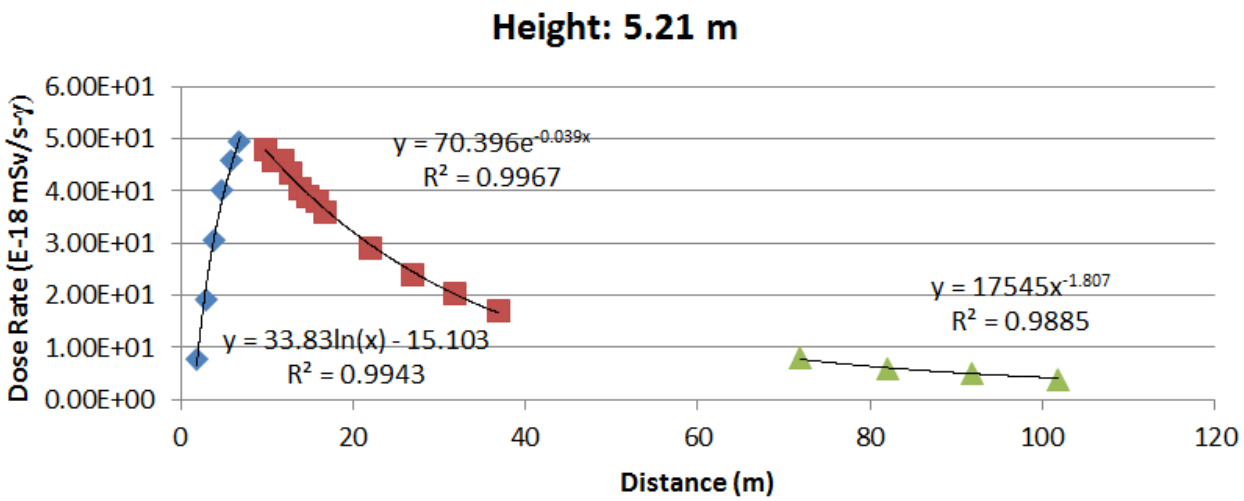

Figure 50 Fitted Dose Rate Profile for West Side at a Height of 5.21 m

South Side

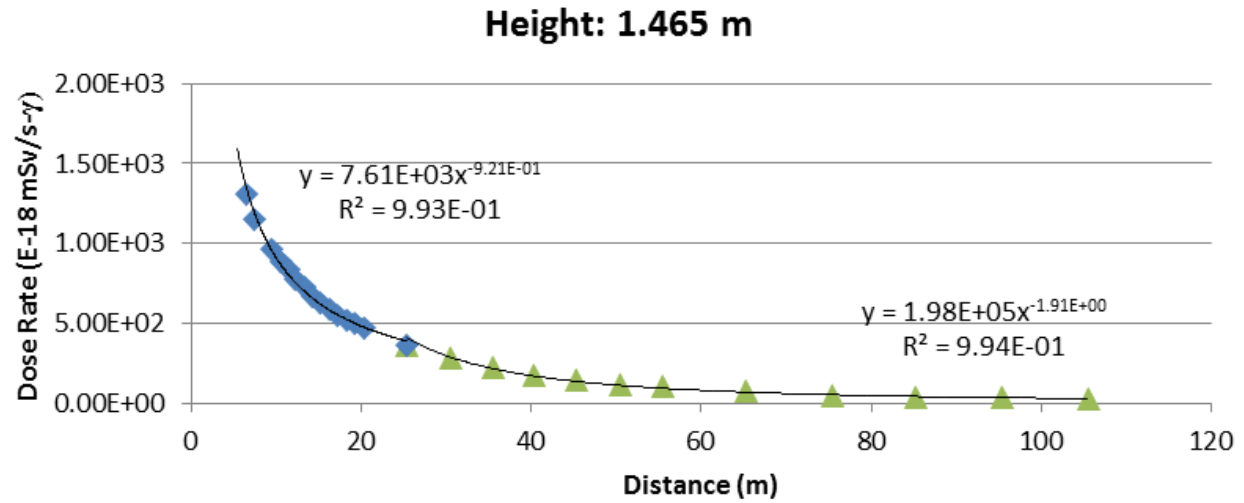

Figure 51 Fitted Dose Rate Profile for South Side at a Height of 1.465 m

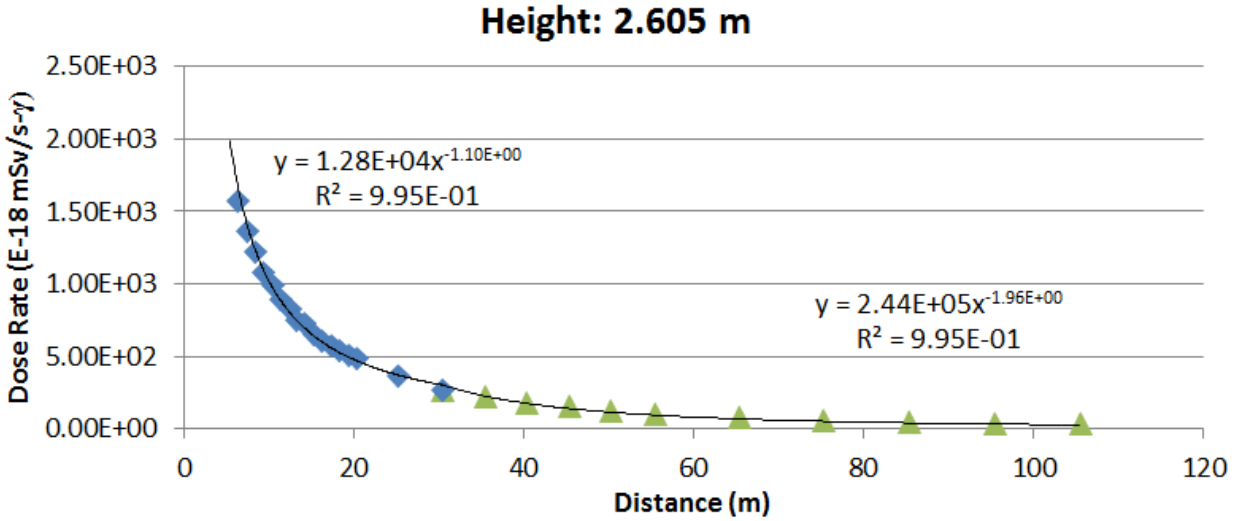

Figure 52 Fitted Dose Rate Profile for South Side at a Height of 2.605 m

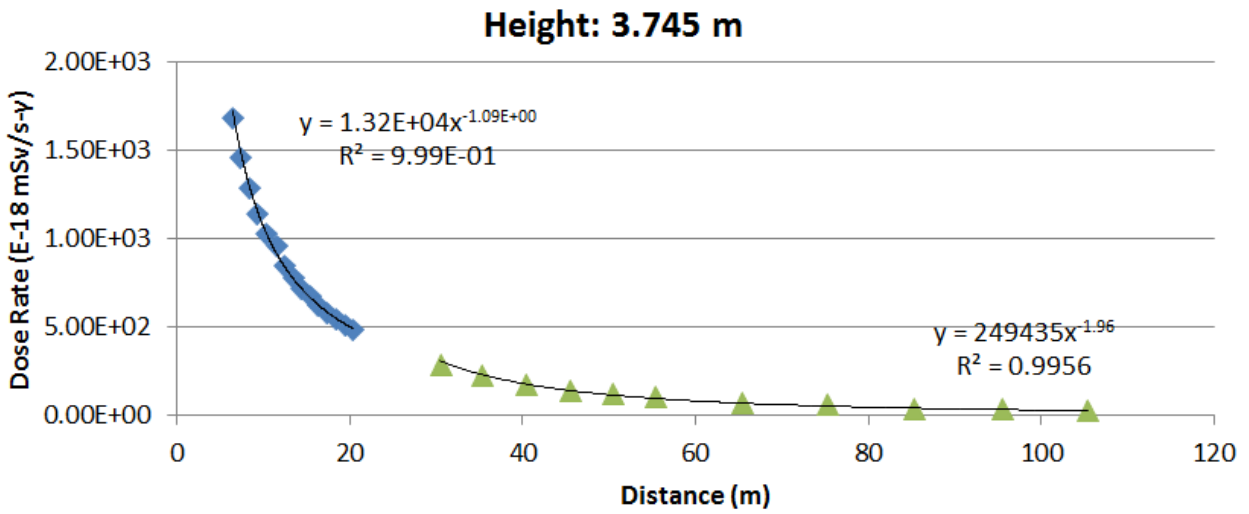

Figure 53 Fitted Dose Rate Profile for South Side at a Height of 3.745 m

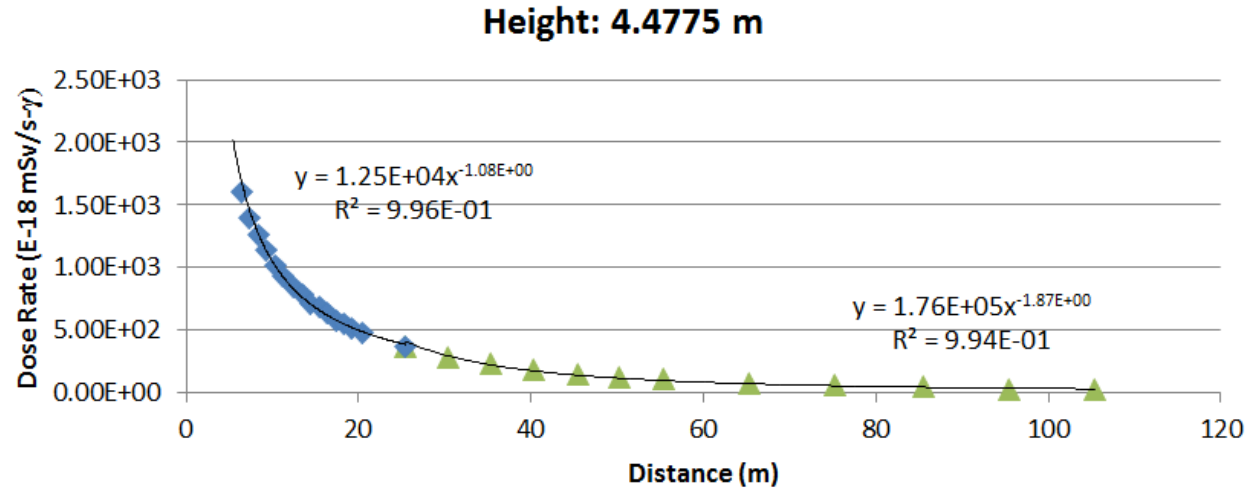

Figure 54 Fitted Dose Rate Profile for South Side at a Height of 4.4775 m

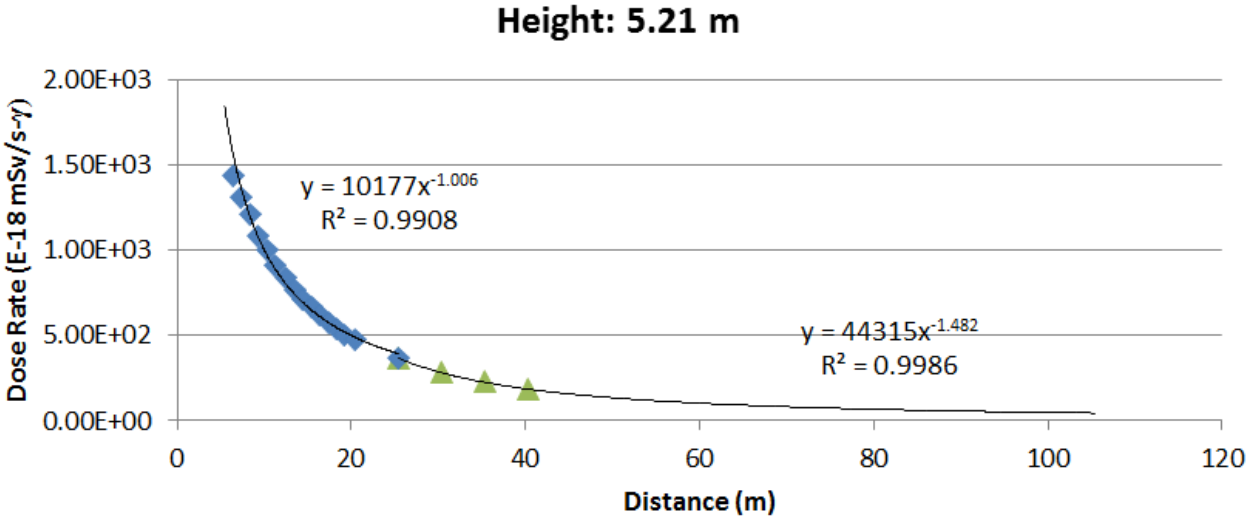

Figure 55 Fitted Dose Rate Profile for South Side at a Height of 5.21 m